J. Fluid Mech. (2022), *vol*. 936, A23, doi:10.1017/jfm.2022.67

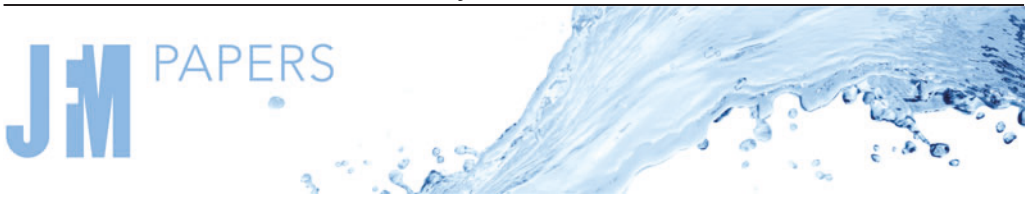

Pressure-driven flow of the viscoelastic Oldroyd-B fluid in narrow non-uniform geometries: analytical results and comparison with simulations

Evgeniy Boyko[1],† **and Howard A. Stone**[1],†

[1]Department of Mechanical and Aerospace Engineering, Princeton University, Princeton, NJ 08544, USA

(Received 11 September 2021; revised 15 November 2021; accepted 18 January 2022)

We analyse the pressure-driven flow of the Oldroyd-B fluid in slowly varying arbitrarily shaped, narrow channels and present a theoretical framework for calculating the relationship between the flow rate q and pressure drop Δp. We first identify the characteristic scales and dimensionless parameters governing the flow in the lubrication limit. Employing a perturbation expansion in powers of the Deborah number (De), we provide analytical expressions for the velocity, stress and the q–Δp relation in the weakly viscoelastic limit up to $O(De^2)$. Furthermore, we exploit the reciprocal theorem derived by Boyko & Stone (*Phys. Rev. Fluids*, vol. 6, 2021, L081301) to obtain the q–Δp relation at the next order, $O(De^3)$, using only the velocity and stress fields at the previous orders. We validate our analytical results with two-dimensional numerical simulations in the case of a hyperbolic, symmetric contracting channel and find excellent agreement. While the velocity remains approximately Newtonian in the weakly viscoelastic limit (i.e. the theorem of Tanner and Pipkin), we reveal that the pressure drop strongly depends on the viscoelastic effects and decreases with De. We elucidate the relative importance of different terms in the momentum equation contributing to the pressure drop along the symmetry line and identify that a pressure drop reduction for narrow contracting geometries is primarily due to gradients in the viscoelastic shear stresses. We further show that, although for narrow geometries the viscoelastic axial stresses are negligible along the symmetry line, they are comparable or larger than shear stresses in the rest of the domain.

Key words: non-Newtonian flows, viscoelasticity, low-Reynolds-number flows

† Email addresses for correspondence: eboyko@princeton.edu, hastone@princeton.edu

1. Introduction

Pressure-driven flows of viscoelastic polymer solutions in narrow non-uniform geometries are widely encountered in industrial processes, such as extrusion (Pearson 1985; Tadmor & Gogos 2013), and in various applications ranging from microfluidic extensional rheometers (Ober *et al.* 2013) to devices for subcutaneous drug administration, in which the liquid may exhibit non-Newtonian behaviour (Allmendinger *et al.* 2014; Fischer *et al.* 2015). The complex rheological behaviour of viscoelastic fluids affects the hydrodynamic features of such flows, including the relationship between the pressure drop Δp across the channel and the flow rate q even at low Reynolds number.

The dependence of the pressure drop on the flow rate of viscoelastic fluids at low Reynolds number has been studied extensively in various geometries. Table 1 lists a chronological selection of previous work on the q–Δp relation for viscoelastic fluids in non-uniform geometries and clearly illustrates that the vast majority of the previous work involved numerical simulations and experimental measurements.

The early studies on the flow rate–pressure drop relation have mainly investigated abrupt geometries such as contraction and contraction–expansion channels. For such geometries, the two-dimensional (2-D) and axisymmetric numerical simulations with constitutive models, such as the Oldroyd-B model and finite-extensibility nonlinear elastic (FENE-CR) model introduced by Chilcott & Rallison (1988), have generally predicted a reduction in the pressure drop with increasing Weissenberg (Wi) or Deborah (De) numbers, which are defined in § 2.1 (Keiller 1993; Szabo *et al.* 1997; Aboubacar *et al.* 2002; Alves *et al.* 2003; Binding *et al.* 2006; Oliveira *et al.* 2007; Aguayo *et al.* 2008; Tamaddon-Jahromi *et al.* 2010, 2011). The exceptions are simulations with small values of the finite extensibility parameter in the FENE-CR model that have reported an initial decrease in the pressure drop followed by a slight increase of the order of 10 % (Szabo *et al.* 1997; Tamaddon-Jahromi *et al.* 2010, 2011). However, these predictions are in contrast with the experimental results of Rothstein & McKinley (1999, 2001), Nigen & Walters (2002) and Sousa *et al.* (2009) for the flow of a polymer solution (Boger fluid) through abrupt axisymmetric contraction–expansion and contraction geometries that have reported a nonlinear increase in the pressure drop with the flow rate. Such an increase in the pressure drop was observed also in experimental studies on microfluidic rectifiers, which further showed the dependence of the flow rate–pressure drop relation on the flow direction (Groisman & Quake 2004; Nguyen *et al.* 2008; Sousa *et al.* 2010).

It is widely hypothesised that this discrepancy is attributed to the inability of the continuum macroscale constitutive models, such as Oldroyd-B, FENE-CR and the finite-extensibility nonlinear elastic model with the Peterlin approximation (FENE-P), to describe accurately the microscopic features of the polymer solutions (Owens & Phillips 2002; Afonso *et al.* 2011). As shown by Koppol *et al.* (2009), a mesoscopic level, micromechanical description, such as the bead–rod and bead–spring models, can be used to resolve, at least partially, this contradiction. For example, using the mesoscopic bead–spring chain model, Koppol *et al.* (2009) showed an increase in the pressure drop for viscoelastic flow in an axisymmetric contraction–expansion geometry, which is in qualitative agreement with the experiments of Rothstein & McKinley (1999). However, Koppol *et al.* (2009) were not able to observe such an agreement for simulations with the continuum FENE-P model, thus indicating the advantage of mesoscopic over macroscopic simulations.

Nevertheless, it should be noted that, to date, the mesoscopic simulations are still computationally expensive and difficult to perform in complex geometries, requiring refined meshing and time-stepping for accurate viscoelastic predictions (Keunings 2004;

	Focus	Geometry	Fluid/model
Black & Denn (1976)	Theor.	Planar converging channel (sink flow)	UCM
Debbaut *et al.* (1988)	Numer.	Planar and axisymmetric abrupt contraction	Oldroyd-B PTT/Giesekus
Keiller (1993)	Numer.	Planar and axisymmetric abrupt contraction	Oldroyd-B FENE-CR
Szabo, Rallison & Hinch (1997)	Numer.	Axisymmetric abrupt contraction–expansion	FENE-CR
Rothstein & McKinley (1999) Rothstein & McKinley (2001)	Exptl.	Axisymmetric abrupt contraction–expansion	Boger fluid
Nigen & Walters (2002)	Exptl.	Three-dimensional and axisymmetric abrupt contraction	Boger fluid
Aboubacar *et al.* (2002)	Numer.	Planar abrupt contraction	Oldroyd-B/PTT
Alves *et al.* (2003)	Numer.	Planar abrupt contraction	Oldroyd-B/PTT
Groisman & Quake (2004)	Exptl.	Microfluidic rectifier consisting of 43 tapered contractions	Boger fluid
Binding *et al.* (2006)	Numer.	Planar and axisymmetric abrupt contraction, expansion and contraction–expansion	Oldroyd-B
Oliveira *et al.* (2007)	Numer.	Axisymmetric abrupt contraction	Oldroyd-B/PTT
Aguayo *et al.* (2008)	Numer.	Planar and axisymmetric abrupt contraction and contraction–expansion	Oldroyd-B
Nguyen *et al.* (2008)	Exptl.	Microfluidic rectifier consisting of several tapered contractions	Boger fluid
Koppol *et al.* (2009)	Numer.	Axisymmetric abrupt contraction–expansion	FENE-P FENE bead-spring chain
Sousa *et al.* (2010)	Exptl.	Microfluidic rectifier consisting of several tapered or hyperbolic contractions	Boger and shear-thinning fluids
Tamaddon-Jahromi *et al.* (2010)	Numer.	Axisymmetric abrupt contraction–expansion	FENE-CR
Tamaddon-Jahromi *et al.* (2011)			Oldroyd-B/PTT
Campo-Deaño *et al.* (2011)	Exptl.	Three-dimensional hyperbolic contraction followed by an abrupt expansion	Boger fluid
Nyström *et al.* (2012)	Numer.	Axisymmetric abrupt and hyperbolic contraction	FENE-CR
Ober *et al.* (2013)	Exptl.	Three-dimensional hyperbolic contraction–expansion	Boger and shear-thinning fluids
Tamaddon-Jahromi *et al.* (2016)	Numer.	Axisymmetric abrupt contraction–expansion	FENE-CR WM-FENE-CR
Nyström *et al.* (2016)	Numer./ Exptl.	Axisymmetric hyperbolic contraction–expansion	WM-FENE-CR
Nyström *et al.* (2017)	Numer./ Exptl.	Axisymmetric hyperbolic contraction	Oldroyd-B FENE-CR/PTT
López-Aguilar *et al.* (2016) Tamaddon-Jahromi *et al.* (2018)	Numer.	Planar and axisymmetric abrupt contraction	WM-FENE-CR
Pérez-Salas *et al.* (2019)	Theor./ Numer.	Planar hyperbolic contraction	PTT with no solvent contrib.
James & Roos (2021)	Exptl.	Axisymmetric hyperbolic contraction	Boger fluid
Present work	Theor.	Planar narrow slowly spatially varying geometries of arbitrary shape	Oldroyd-B

Table 1. Chronological selection of previous experimental, numerical and theoretical papers on the flow rate–pressure drop relation for the low-Reynolds-number flows of viscoelastic fluids in non-uniform geometries.

Afonso *et al.* 2011; Alves, Oliveira & Pinho 2021). Therefore, despite the limitations of a continuum approach, the vast majority of studies in non-Newtonian fluid mechanics still exploit the macroscopic constitutive equations, such as Oldroyd-B, FENE-CR and FENE-P, which, in principle, can be modified to incorporate some microscopic features. For instance, Webster and co-workers proposed a new constitutive equation, which is the hybrid combination of White and Metzner (White & Metzner 1963) and FENE-CR models (WM-FENE-CR; see, e.g., Tamaddon-Jahromi *et al.* 2011, 2016; Webster *et al.* 2019). Specifically, in this model, the deviatoric stress tensor $\boldsymbol{\tau}$, which is the sum of the Newtonian solvent and viscoelastic polymer contributions, is obtained by multiplying the expression for $\boldsymbol{\tau}$ from the FENE-CR model by a dissipative function $\phi(\dot{\varepsilon})$, usually taken as $\phi(\dot{\varepsilon}) = 1 + (\lambda_D \dot{\varepsilon})^2$, where λ_D is an additional time constant and $\dot{\varepsilon} = 3\boldsymbol{III}_E/\boldsymbol{II}_E$ is the generalised extension rate based on the second and third invariants of the rate-of-strain tensor $\boldsymbol{E}$ defined in § 2.1, wherein $\boldsymbol{II}_E = \mathrm{tr}(\boldsymbol{E}^2)/2$ and $\boldsymbol{III}_E = \det(\boldsymbol{E})$ (Tamaddon-Jahromi *et al.* 2016). Such a model exhibits a constant shear viscosity, finite extensibility with a bounded extensional viscosity that reaches an ultimate plateau, and a first-normal stress-difference that has a weaker than quadratic dependence on the shear rate in the Oldroyd-B model. Using this hybrid WM-FENE-CR model, Webster and co-workers were able to achieve quantitative agreement between their numerical predictions for the pressure drop and the earlier experiments of Rothstein & McKinley (2001) and Nigen & Walters (2002), where λ_D and finite extensibility served as fitting parameters (López-Aguilar *et al.* 2016; Tamaddon-Jahromi *et al.* 2016, 2018).

After primarily focusing on abrupt contractions or contraction–expansions geometries a decade ago, hyperbolic symmetric channels with nearly constant extensional rates along the centreline have also received much attention, and several groups suggested to use of hyperbolic geometries for obtaining extensional properties of viscoelastic fluids through q–Δp measurements (Campo-Deaño *et al.* 2011; Nyström *et al.* 2012, 2016, 2017; Ober *et al.* 2013; Keshavarz & McKinley 2016; Zografos *et al.* 2020). However, recently some researchers conjectured that, given the complex mixture of shear and extensional flow components in this geometry, it is difficult to determine extensional viscosity directly from q–Δp data (James 2016; Hsiao *et al.* 2017).

Of particular interest is a recent experimental study of James & Roos (2021) on the pressure-driven flow of Boger fluids through a long hyperbolic contracting channel. James & Roos (2021) measured the pressure drop for various flow rates and found that the pressure drop matches equivalent Newtonian measurements, in contrast to previous experimental results showing a nonlinear increase in the pressure drop with the flow rate (see, e.g., Rothstein & McKinley 1999, 2001; Campo-Deaño *et al.* 2011; Ober *et al.* 2013). The explanation for this discrepancy lies in the different pressure drops measured by the different sets of authors. The experimental set-up of James & Roos (2021) consisted of a hyperbolic contracting channel connected upstream to a long straight channel. The fluid was driven by pressurised air to flow through a straight section, entered the contracting channel and then exited to the atmosphere. James & Roos (2021) defined the pressure drop as the difference between the air pressure required to drive the fluid through a straight section and the atmospheric pressure at the end of the channel, where die swell occurred.

In contrast to pressure drop measurements of James & Roos (2021) that included the apparent exit effects, most of the previous experimental studies eliminated the entrance and exit effects (see, e.g., Rothstein & McKinley 1999, 2001; Campo-Deaño *et al.* 2011; Ober *et al.* 2013). For example, the experimental set-up of Rothstein & McKinley (1999) consisted of two long straight channels connected to the non-uniform region upstream and downstream, and the pressure drop was measured in these straight channels far from the

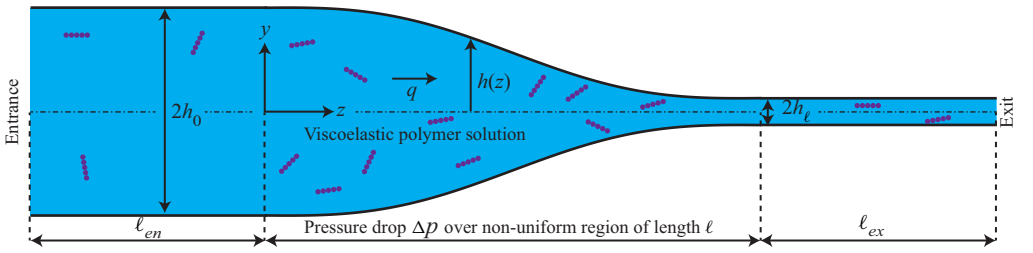

Figure 1. Schematic illustration of the 2-D configuration consisting of a slowly spatially varying and symmetric channel of height $2h(z)$ and length ℓ ($h \ll \ell$), connected to two long straight channels of height $2h_0$ and $2h_\ell$, respectively. The configuration contains a viscoelastic dilute polymer solution steadily driven by the imposed flow rate q. We are interested in determining the pressure drop Δp over a streamwise distance ℓ, arising from the non-uniformity of geometry, while eliminating the entrance and exit effects.

entrance and exit. In this work, we follow the study of Rothstein & McKinley (1999) and explore the pressure drop originating from the non-uniformity of geometry while eliminating the entrance and exit effects (see figure 1).

It should be noted that, in addition to abrupt contracting and hyperbolic channels, the flow rate–pressure drop relation of viscoelastic fluids has been studied in other geometries, such as converging (Black & Denn 1976) and undulating (Pilitsis & Beris 1989; Souvaliotis & Beris 1992) channels. For example, Black & Denn (1976) studied the pressure-driven flow of the upper-convected Maxwell (UCM) fluid in a rectilinearly converging channel. Applying the sink flow approximation and assuming a weakly viscoelastic limit, Black & Denn (1976) provided a perturbation solution to the flow field up to second order in Weissenberg number. Black & Denn (1976) also depicted the first three terms of a perturbation solution for the power required to drive the fluid as a function of Wi, indicating that the first viscoelastic correction decreases the power or pressure drop. However, no explicit expressions nor validation of this result by comparison with simulations has been presented. In addition, Pilitsis & Beris (1989) studied numerically the pressure-driven flow of the UCM and Oldroyd-B fluids in an undulating cylinder and showed a small reduction in the hydrodynamic resistance, defined as a ratio of the pressure drop to the flow rate, with increasing Weissenberg number.

Recently, Pérez-Salas *et al.* (2019) studied analytically and numerically the pressure-driven flow of a Phan-Thien–Tanner (PTT) fluid (Phan-Thien & Tanner 1977; Phan-Thien 1978) through a planar hyperbolic contraction. Using lubrication theory and neglecting the solvent contribution, Pérez-Salas *et al.* (2019) derived closed-form expressions for the non-dimensional velocity and pressure fields, which depend on the channel geometry and the product $\varepsilon_{PTT} Wi^2$, where ε_{PTT} is the extensibility parameter of the PTT model. Their results predicted a decrease in the pressure drop with increasing Wi. However, such a reduction in the pressure drop arises due to shear-thinning effects of the PTT fluid, which are manifested when Wi increases. Moreover, for $\varepsilon_{PTT} = 0$, corresponding to the Oldroyd-B model, the solution of Pérez-Salas *et al.* (2019) reduces to the Newtonian solution, which is independent of Wi.

In the context of lubrication theory, it is worth mentioning earlier studies on the pressure-driven flow of a fibre suspension in a slowly varying channel, which showed the ability of the lubrication approach to capture well the flow field (Rallison & Keiller 1993; Sykes & Rallison 1997). We have recently exploited the Lorentz reciprocal theorem and lubrication theory to derive a closed-form expression for the flow rate–pressure drop relation for complex fluids in narrow geometries, which holds for a wide class of non-Newtonian constitutive models (Boyko & Stone 2021). We showed the use of our

theory to calculate analytically the first-order non-Newtonian correction for the q–Δp relation for the viscoelastic second-order fluid and shear-thinning Carreau fluid, solely using the corresponding Newtonian solution and bypassing solution of the non-Newtonian flow problem.

To the best of the authors' knowledge, no analytical solution for the q–Δp relation for constant shear-viscosity viscoelastic (Boger) fluids in narrow geometries has been reported in the literature, even for 'simple' models such as Oldroyd-B and FENE-CR in the weakly viscoelastic limit. Such analytical solutions, however, are of fundamental importance as they may be used directly for comparison with experimental data and, in the case of discrepancy between the theory and experiments, may provide insight into the cause of this disagreement and the adequacy of the constitutive model.

In this work, we provide a theoretical framework for calculating the flow rate–pressure drop relation of viscoelastic fluids in narrow channels of slowly varying arbitrary shapes. The present work presents analytical results for velocity and pressure fields and the q–Δp relation for the Oldroyd-B model in the weakly viscoelastic limit. In subsequent work, we will analyse more complex constitutive models, incorporating additional microscopic features of polymer solutions. Our approach for obtaining analytical solutions for velocity and pressure is motivated by studies on thin films and lubrication problems (Tichy 1996; Zhang, Matar & Craster 2002; Saprykin, Koopmans & Kalliadasis 2007; Ahmed & Biancofiore 2021). Such an approach relies on exploiting the narrowness of the geometry through the application of the lubrication approximation and a perturbation expansion in powers of the Deborah number De, which is assumed to be small, $De \ll 1$, and solving order by order, often resulting in cumbersome calculations at high orders. Instead, once the velocity at $O(De^2)$ is obtained, we use the reciprocal theorem, recently derived by Boyko & Stone (2021), to calculate the pressure drop at $O(De^3)$, bypassing the detailed calculations of the viscoelastic flow problem at this order and relying only on the solution from previous orders. To validate the analytical results of our model, we perform 2-D finite-element numerical simulations with the Oldroyd-B model and find a good agreement between the theory and simulations, even for the cases when the hypotheses behind the lubrication approximation are not strictly satisfied. Given the recognised shortcomings of the Oldroyd-B and commonly used continuum finite-extensibility nonlinear elastic (FENE) models in predicting the experimental observations for the flow rate–pressure drop relation, we are hopeful that the insights presented here may be useful in understanding possible physical or molecularly inspired modifications to the constitutive descriptions to improve future modeling and simulation efforts.

The paper is organised as follows. In § 2, we present the problem formulation and the dimensional governing equations and boundary conditions for the pressure-driven flow of the Oldroyd-B fluid. We further identify the characteristic scales and dimensionless parameters governing the flow and provide the non-dimensional governing equations. In § 3, we present a low-Deborah-number lubrication analysis and derive closed-form analytical solutions for the flow field and pressure drop up to $O(De^2)$. Exploiting the reciprocal theorem, in § 4 we calculate the pressure drop at $O(De^3)$, relying only on the solutions from previous orders. We present the results in § 5, including a comparison between the analytical predictions and the 2-D numerical simulations, finding excellent agreement between the two approaches. We conclude with a discussion of the results in § 6.

2. Problem formulation and governing equations

We study the incompressible steady flow of a non-Newtonian viscoelastic dilute polymer solution in a slowly spatially varying and symmetric 2-D channel of height $2h(z)$ and

length ℓ, where $h \ll \ell$. We assume that the imposed flow rate q (per unit depth) induces the fluid motion with pressure distribution p and velocity $\boldsymbol{u} = (u_z, u_y)$. Our primary interest is to determine, for a non-uniform geometry, the pressure drop Δp over a streamwise distance ℓ, while eliminating the entrance and exit effects. To this end, motivated by the geometries used in previous experimental and numerical studies (see, e.g., Szabo *et al.* 1997; Rothstein & McKinley 1999; Alves *et al.* 2003; Alves & Poole 2007; Campo-Deaño *et al.* 2011; Ober *et al.* 2013; Zografos *et al.* 2020; Zargartalebi, Zargartalebi & Benneker 2021), we assume that the inlet ($z = 0$) and outlet ($z = \ell$) of the non-uniform region are connected to two long straight channels of height $2h_0$ and $2h_\ell$, and length ℓ_{en} and ℓ_{ex}, respectively. Consequently, the flow is fully developed at the inlet of the non-uniform region and becomes fully developed again towards the exit of the configuration. Figure 1 presents a schematic illustration of the 2-D configuration and the coordinate system (y, z), whose z axes lies in the symmetry midplane of the channel and y is in the direction of the shortest dimension. It should be noted that when a viscoelastic fluid exits from the non-uniform region directly to the atmosphere or a large reservoir, there can be significant exit effects due to axial stresses (James & Roos 2021).

While throughout this work we consider steady and stable flows, it should be noted that the flow of viscoelastic fluids within non-uniform geometries may become unstable above a certain flow rate even at low Reynolds numbers due to the fluid's complex rheology (Larson 1992; Shaqfeh 1996; Datta *et al.* 2021; Steinberg 2021). We consider low-Reynolds-number flows, so that the fluid inertia is negligible relative to viscous stresses. In this limit, the fluid motion is governed by the continuity and momentum equations

$$\boldsymbol{\nabla} \cdot \boldsymbol{u} = 0, \quad \boldsymbol{\nabla} \cdot \boldsymbol{\sigma} = \boldsymbol{0}, \tag{2.1a,b}$$

where $\boldsymbol{\sigma}$ is the stress tensor given by

$$\boldsymbol{\sigma} = -p\boldsymbol{I} + 2\eta_s \boldsymbol{E} + \boldsymbol{\tau}_p. \tag{2.2}$$

The first term on the right-hand side of (2.2) is the pressure contribution, the second term is the viscous stress contribution of Newtonian solvent with a constant viscosity η_s, where $\boldsymbol{E} = (\boldsymbol{\nabla u} + (\boldsymbol{\nabla u})^{\mathrm{T}})/2$ is the rate-of-strain tensor, and the last term, $\boldsymbol{\tau}_p$, is the polymer contribution to the stress tensor.

In this work, we describe the viscoelastic behaviour of the polymer solution using the Oldroyd-B constitutive model (Bird, Armstrong & Hassager 1987). This is a widely used continuum model for Boger fluids, characterised by a constant shear viscosity. The Oldroyd-B equation can be derived from microscopic principles by modeling the polymer molecules as dumbbells, which follow a linear Hooke's law for the restoring force as they are advected and stretched by the flow. In the Oldroyd-B model, the polymer contribution to the stress tensor $\boldsymbol{\tau}_p$ can be expressed in the form (Bird *et al.* 1987; Morozov & Spagnolie 2015; Alves *et al.* 2021)

$$\boldsymbol{\tau}_p = \frac{\eta_p}{\lambda}(\boldsymbol{A} - \boldsymbol{I}), \tag{2.3}$$

where η_p is the polymer contribution to the shear viscosity at zero shear rate and λ is the longest relaxation time of the polymers. In (2.3), $\boldsymbol{A}$ is the conformation tensor of the dumbbells, which denotes the ensemble average of the second moment of the dumbbell end-to-end vector $\boldsymbol{r}$ (scaled with its equilibrium value), $\boldsymbol{A} \equiv \langle \boldsymbol{rr} \rangle$, and evolves at steady

state according to (Bird *et al.* 1987; Morozov & Spagnolie 2015; Alves *et al.* 2021)

$$\boldsymbol{u}\cdot\nabla\boldsymbol{A}-(\nabla\boldsymbol{u})^{\mathrm{T}}\cdot\boldsymbol{A}-\boldsymbol{A}\cdot(\nabla\boldsymbol{u})=-\frac{1}{\lambda}(\boldsymbol{A}-\boldsymbol{I}). \tag{2.4}$$

Combining (2.3) and (2.4), we obtain an evolution equation for the polymer contribution to the stress tensor $\boldsymbol{\tau}_p$, given at steady state as (Bird *et al.* 1987; Morozov & Spagnolie 2015; Alves *et al.* 2021),

$$\boldsymbol{\tau}_p+\lambda[\boldsymbol{u}\cdot\nabla\boldsymbol{\tau}_p-(\nabla\boldsymbol{u})^{\mathrm{T}}\cdot\boldsymbol{\tau}_p-\boldsymbol{\tau}_p\cdot(\nabla\boldsymbol{u})]=2\eta_p\boldsymbol{E}. \tag{2.5}$$

Using (2.2), (2.3) and (2.5), the stress tensor $\boldsymbol{\sigma}$ can be also expressed as

$$\boldsymbol{\sigma}=-p\boldsymbol{I}+2\eta_0\boldsymbol{E}+\eta_p\boldsymbol{S}, \tag{2.6}$$

where $\eta_0=\eta_s+\eta_p$ is the total zero-shear-rate viscosity of the polymer solution and $\boldsymbol{S}$ is defined through $\boldsymbol{\tau}_p=2\eta_p\boldsymbol{E}+\eta_p\boldsymbol{S}$, so that

$$\begin{aligned}\boldsymbol{S}&=-\frac{\lambda}{\eta_p}[\boldsymbol{u}\cdot\nabla\boldsymbol{\tau}_p-(\nabla\boldsymbol{u})^{\mathrm{T}}\cdot\boldsymbol{\tau}_p-\boldsymbol{\tau}_p\cdot(\nabla\boldsymbol{u})]\\&=-[\boldsymbol{u}\cdot\nabla\boldsymbol{A}-(\nabla\boldsymbol{u})^{\mathrm{T}}\cdot(\boldsymbol{A}-\boldsymbol{I})-(\boldsymbol{A}-\boldsymbol{I})\cdot(\nabla\boldsymbol{u})].\end{aligned} \tag{2.7}$$

Substituting (2.6) into (2.1) provides an alternative form of the governing equations

$$\nabla\cdot\boldsymbol{u}=0,\quad \nabla p=\eta_0\nabla^2\boldsymbol{u}+\eta_p\nabla\cdot\boldsymbol{S}, \tag{2.8a,b}$$

which is convenient for assessing the viscoelastic effects on the flow and pressure fields, where $\boldsymbol{S}$ is given in (2.7) and $\boldsymbol{A}$ evolves according to (2.4).

The governing equations (2.1)–(2.8) are supplemented by the boundary conditions

$$u_z(h(z),z)=0,\quad u_y(h(z),z)=0,\quad \frac{\partial u_z}{\partial y}(0,z)=0, \tag{2.9a–c}$$

$$u_z(y,-\ell_{en})=\frac{3q}{4}\frac{h_0^2-y^2}{h_0^3},\quad u_z(y,\ell+\ell_{ex})=\frac{3q}{4}\frac{h_\ell^2-y^2}{h_\ell^3}, \tag{2.9d,e}$$

$$A_{zz}(y,-\ell_{en})=1+\frac{9}{2}\left(\frac{\lambda qy}{h_0^3}\right)^2,\quad A_{yz}(y,-\ell_{en})=-\frac{3\lambda qy}{2h_0^3},\quad A_{yy}(y,-\ell_{en})=1. \tag{2.9f–h}$$

The first three boundary conditions (2.9*a–c*) correspond to the no-slip and no-penetration boundary conditions along the channel walls and the symmetry boundary condition at the centreline, respectively. Equations (2.9*d*,*e*) correspond to the fully developed unidirectional Poiseuille velocity profile at the entrance and exit. These two boundary conditions ensure that the integral constraint $2\int_0^{h(z)}u_z(y,z)\,\mathrm{d}y=q$ is satisfied along the channel. In addition, at the entrance, we impose the polymer stress (or conformation tensor) distribution corresponding to the Poiseuille flow, as given in (2.9*a–c*) to (2.9*f–h*) (Szabo *et al.* 1997; Koppol *et al.* 2009). In addition, at the exit, the reference value for the pressure is set to zero on $y=0$.

2.1. *Scaling analysis and non-dimensionalisation*

In this work, we examine narrow configurations, in which $h(z) \ll \ell$, h_ℓ is the half-height at $z = \ell$ and $u_c = q/2h_\ell$ is the characteristic velocity scale set by the cross-sectionally averaged velocity. Note that for the 2-D case, the flow rate q is per unit depth.

We introduce non-dimensional variables based on lubrication theory (Tichy 1996; Zhang *et al.* 2002; Saprykin *et al.* 2007; Ahmed & Biancofiore 2021),

$$Z = \frac{z}{\ell}, \quad Y = \frac{y}{h_\ell}, \quad U_z = \frac{u_z}{u_c}, \quad U_y = \frac{u_y}{\epsilon u_c}, \tag{2.10a}$$

$$P = \frac{p}{\eta_0 u_c \ell / h_\ell^2}, \quad \Delta P = \frac{\Delta p}{\eta_0 u_c \ell / h_\ell^2}, \quad H = \frac{h}{h_\ell}, \tag{2.10b}$$

$$\mathcal{T}_{p,zz} = \frac{\epsilon^2 \ell}{\eta_0 u_c} \tau_{p,zz}, \quad \tilde{A}_{zz} = \frac{\epsilon^2 (A_{zz} - 1)}{De}, \quad \mathcal{S}_{zz} = \frac{\epsilon^2 \ell}{u_c De} S_{zz}, \tag{2.10c}$$

$$\mathcal{T}_{p,yz} = \frac{\epsilon \ell}{\eta_0 u_c} \tau_{p,yz}, \quad \tilde{A}_{yz} = \frac{\epsilon A_{yz}}{De}, \quad \mathcal{S}_{yz} = \frac{\epsilon \ell}{u_c De} S_{yz}, \tag{2.10d}$$

$$\mathcal{T}_{p,yy} = \frac{\ell}{\eta_0 u_c} \tau_{p,yy}, \quad \tilde{A}_{yy} = \frac{A_{yy} - 1}{De}, \quad \mathcal{S}_{yy} = \frac{\ell}{u_c De} S_{yy}, \tag{2.10e}$$

where we have introduced the aspect ratio of the configuration, which is assumed to be small,

$$\epsilon = \frac{h_\ell}{\ell} \ll 1, \tag{2.11}$$

the viscosity ratios,

$$\tilde{\beta} = \frac{\eta_p}{\eta_s + \eta_p} = \frac{\eta_p}{\eta_0} \quad \text{and} \quad \beta = 1 - \tilde{\beta} = \frac{\eta_s}{\eta_0}, \tag{2.12a,b}$$

and the Deborah and Weissenberg numbers,

$$De = \frac{\lambda u_c}{\ell} \quad \text{and} \quad Wi = \frac{\lambda u_c}{h_\ell}. \tag{2.13a,b}$$

The non-dimensional shape of the channel is denoted by $H(Z)$ and is an important parameter in our analysis.

Following Ahmed & Biancofiore (2021), we define the Deborah number De as the ratio of the polymer relaxation time, λ, to the residence time in the spatially non-uniform region, ℓ/u_c, or alternatively, as the product of the relaxation time scale of the fluid and the characteristic extensional rate of the flow (see also Tichy 1996; Zhang *et al.* 2002; Saprykin *et al.* 2007). The Weissenberg number Wi is the product of the relaxation time scale of the fluid and the characteristic shear rate of the flow, and is related to the Deborah number through $De = \epsilon Wi$ (Ahmed & Biancofiore 2021). We note that since we assume $\epsilon \ll 1$, De can be small while keeping $Wi = O(1)$.

2.2. *Governing equations in dimensionless form*

Using the non-dimensionalisation (2.10)–(2.13), the governing equations (2.1)–(2.9) take the form

$$\frac{\partial U_z}{\partial Z} + \frac{\partial U_y}{\partial Y} = 0, \tag{2.14a}$$

$$\frac{\partial P}{\partial Z} = \epsilon^2 \frac{\partial^2 U_z}{\partial Z^2} + \frac{\partial^2 U_z}{\partial Y^2} + \tilde{\beta} De \frac{\partial \mathcal{S}_{zz}}{\partial Z} + \tilde{\beta} De \frac{\partial \mathcal{S}_{yz}}{\partial Y}, \tag{2.14b}$$

$$\frac{\partial P}{\partial Y} = \epsilon^4 \frac{\partial^2 U_y}{\partial Z^2} + \epsilon^2 \frac{\partial^2 U_y}{\partial Y^2} + \epsilon^2 \tilde{\beta} De \frac{\partial \mathcal{S}_{yz}}{\partial Z} + \epsilon^2 \tilde{\beta} De \frac{\partial \mathcal{S}_{yy}}{\partial Y}, \tag{2.14c}$$

$$De \left(U_z \frac{\partial A_{zz}}{\partial Z} + U_y \frac{\partial A_{zz}}{\partial Y} - 2 \frac{\partial U_z}{\partial Z} A_{zz} - 2 \frac{\partial U_z}{\partial Y} A_{yz} \right) - 2\epsilon^2 \frac{\partial U_z}{\partial Z} = -A_{zz}, \tag{2.14d}$$

$$De \left(U_z \frac{\partial A_{yy}}{\partial Z} + U_y \frac{\partial A_{yy}}{\partial Y} - 2 \frac{\partial U_y}{\partial Z} A_{yz} - 2 \frac{\partial U_y}{\partial Y} A_{yy} \right) - 2 \frac{\partial U_y}{\partial Y} = -A_{yy}, \tag{2.14e}$$

$$De \left(U_z \frac{\partial A_{yz}}{\partial Z} + U_y \frac{\partial A_{yz}}{\partial Y} - \frac{\partial U_y}{\partial Z} A_{zz} - \frac{\partial U_z}{\partial Y} A_{yy} \right) - \epsilon^2 \frac{\partial U_y}{\partial Z} - \frac{\partial U_z}{\partial Y} = -A_{yz}, \tag{2.14f}$$

where we dropped tildes in the components of $\boldsymbol{A}$ for simplicity. From (2.14*c*), it follows that $P = P(Z) + O(\epsilon^2)$, i.e. the pressure is independent of Y up to $O(\epsilon^2)$, consistent with the classical lubrication approximation.

The explicit expressions for $\mathcal{S}_{zz}$ and $\mathcal{S}_{yz}$ appearing in (2.14*b*) are

$$\mathcal{S}_{zz} = -\left(U_z \frac{\partial A_{zz}}{\partial Z} + U_y \frac{\partial A_{zz}}{\partial Y} - 2 \frac{\partial U_z}{\partial Z} A_{zz} - 2 \frac{\partial U_z}{\partial Y} A_{yz} \right), \tag{2.15a}$$

$$\mathcal{S}_{yz} = -\left(U_z \frac{\partial A_{yz}}{\partial Z} + U_y \frac{\partial A_{yz}}{\partial Y} - \frac{\partial U_y}{\partial Z} A_{zz} - \frac{\partial U_z}{\partial Y} A_{yy} \right), \tag{2.15b}$$

and they are related to A_{zz} and A_{yz} through

$$A_{zz} = De \mathcal{S}_{zz} + O(\epsilon^2), \quad A_{yz} = De \mathcal{S}_{yz} + \frac{\partial U_z}{\partial Y} + O(\epsilon^2), \tag{2.16a}$$

and to $\mathcal{T}_{p,zz}$ and $\mathcal{T}_{p,yz}$ through

$$\mathcal{T}_{p,zz} = \tilde{\beta} De \mathcal{S}_{zz} + O(\epsilon^2), \quad \mathcal{T}_{p,yz} = \tilde{\beta} De \mathcal{S}_{yz} + \tilde{\beta} \frac{\partial U_z}{\partial Y} + O(\epsilon^2). \tag{2.16b}$$

3. Low-Deborah-number lubrication analysis

In the previous section we obtained the non-dimensional equations (2.14), which are governed by the three non-dimensional parameters: $\tilde{\beta}$, De and ϵ^2, where $\epsilon = h_\ell/\ell \ll 1$. In this section, we consider the weakly viscoelastic limit, $De \ll 1$, and exploit the narrowness of the geometry, $\epsilon \ll 1$, to derive analytical expressions for the velocity field and the q–Δp relation for the pressure-driven flow of the Oldroyd-B model in a non-uniform channel of arbitrary shape $H(Z)$. We assume $\eta_p < \eta_s$, thus implying a dilute polymer solution with $\tilde{\beta} = \eta_p/\eta_0 < 1/2$ (Groisman & Steinberg 1996; Groisman & Quake 2004). To this end,

we seek solutions of the form

$$\begin{pmatrix} U_z \\ U_y \\ P \\ A_{zz} \\ A_{yy} \\ A_{yz} \end{pmatrix} = \begin{pmatrix} U_{z,0} \\ U_{y,0} \\ P_0 \\ A_{zz,0} \\ A_{yy,0} \\ A_{yz,0} \end{pmatrix} + De \begin{pmatrix} U_{z,1} \\ U_{y,1} \\ P_1 \\ A_{zz,1} \\ A_{yy,1} \\ A_{yz,1} \end{pmatrix} + De^2 \begin{pmatrix} U_{z,2} \\ U_{y,2} \\ P_2 \\ A_{zz,2} \\ A_{yy,2} \\ A_{yz,2} \end{pmatrix} + O(\epsilon^2, De^3), \tag{3.1}$$

and in the following subsections, we derive asymptotic expressions for the velocity field and the pressure drop up to $O(De^2)$. In § 4, we use reciprocal theorem to calculate the pressure drop at the next order, $O(De^3)$.

We note that in the weakly viscoelastic and lubrication limits, considered here, it is sufficient to apply the boundary conditions,

$$U_z(H(Z), Z) = 0, \quad U_y(H(Z), Z) = 0, \quad \frac{\partial U_z}{\partial Y}(0, Z) = 0, \quad \int_0^{H(Z)} U_z(Y, Z)\,\mathrm{d}Y = 1, \tag{3.2}$$

to determine the flow field and pressure drop, similar to the case of the sink flow of weakly viscoelastic fluids (Black & Denn 1976).

3.1. *Leading-order solution*

Substituting (3.1) into (2.14) and considering the leading order in De, we obtain

$$\frac{\partial U_{z,0}}{\partial Z} + \frac{\partial U_{y,0}}{\partial Y} = 0, \tag{3.3a}$$

$$\frac{\partial P_0}{\partial Z} = \frac{\partial^2 U_{z,0}}{\partial Y^2}, \tag{3.3b}$$

$$\frac{\partial P_0}{\partial Y} = 0, \tag{3.3c}$$

$$A_{zz,0} = 0, \tag{3.3d}$$

$$A_{yy,0} = 2\frac{\partial U_{y,0}}{\partial Y}, \tag{3.3e}$$

$$A_{yz,0} = \frac{\partial U_{z,0}}{\partial Y}, \tag{3.3f}$$

subject to the boundary conditions

$$U_{z,0}(H(Z), Z) = 0, \quad U_{y,0}(H(Z), Z) = 0, \quad \frac{\partial U_{z,0}}{\partial Y}(0, Z) = 0, \quad \int_0^{H(Z)} U_{z,0}(Y, Z)\,\mathrm{d}Y = 1. \tag{3.4a–d}$$

As expected, at the leading order, (3.3b) reduces to the classical momentum equation of the Newtonian fluid with a constant viscosity η_0.

The solution of (3.3*b*) using (3.4*a*) and (3.4*c*) is

$$U_{z,0}(Y,Z) = \frac{1}{2}\frac{\mathrm{d}P_0}{\mathrm{d}Z}(Y^2 - H(Z)^2), \tag{3.5}$$

where the pressure gradient, which only depends on Z, follows from applying the integral constraint (3.4*d*),

$$\frac{\mathrm{d}P_0}{\mathrm{d}Z} = -\frac{3}{H(Z)^3}. \tag{3.6}$$

The corresponding axial velocity distribution is then

$$U_{z,0}(Y,Z) = \frac{3}{2}\frac{(H(Z)^2 - Y^2)}{H(Z)^3}. \tag{3.7}$$

Substituting (3.7) into the continuity equation (3.3*a*) and using (3.4*b*), yields

$$U_{y,0}(Y,Z) = \frac{3}{2}\frac{\mathrm{d}H(Z)}{\mathrm{d}Z}\frac{Y(H(Z)^2 - Y^2)}{H(Z)^4}, \tag{3.8}$$

and thus the yy- and yz-components of the conformation tensor at the leading-order depend on channel shape via

$$A_{yy,0} = \frac{3\mathrm{d}H(Z)}{\mathrm{d}Z}\frac{(-3Y^2 + H(Z)^2)}{H(Z)^4}, \quad A_{yz,0} = -\frac{3Y}{H(Z)^3}. \tag{3.9a,b}$$

Finally, integrating (3.6) with respect to Z from 0 to 1 provides the pressure drop at the leading order,

$$\Delta P_0 = 3\int_0^1 \frac{\mathrm{d}Z}{H(Z)^3}. \tag{3.10}$$

3.2. *First-order solution*

At the first order, $O(De)$, the governing equations (2.14)–(2.15) yield

$$\frac{\partial U_{z,1}}{\partial Z} + \frac{\partial U_{y,1}}{\partial Y} = 0, \tag{3.11a}$$

$$\frac{\partial P_1}{\partial Z} = \frac{\partial^2 U_{z,1}}{\partial Y^2} + \tilde{\beta}\left[\frac{\partial \mathcal{S}_{zz,0}}{\partial Z} + \frac{\partial \mathcal{S}_{yz,0}}{\partial Y}\right], \tag{3.11b}$$

$$\frac{\partial P_1}{\partial Y} = 0, \tag{3.11c}$$

$$2\frac{\partial U_{z,0}}{\partial Y}A_{yz,0} = A_{zz,1}, \tag{3.11d}$$

$$U_{z,0}\frac{\partial A_{yy,0}}{\partial Z} + U_{y,0}\frac{\partial A_{yy,0}}{\partial Y} - 2\frac{\partial U_{y,0}}{\partial Z}A_{yz,0} - 2\frac{\partial U_{y,0}}{\partial Y}A_{yy,0} - 2\frac{\partial U_{y,1}}{\partial Y} = -A_{yy,1}, \tag{3.11e}$$

$$U_{z,0}\frac{\partial A_{yz,0}}{\partial Z} + U_{y,0}\frac{\partial A_{yz,0}}{\partial Y} - \frac{\partial U_{z,0}}{\partial Y}A_{yy,0} - \frac{\partial U_{z,1}}{\partial Y} = -A_{yz,1}, \tag{3.11f}$$

$$\mathcal{S}_{zz,0} = 2\frac{\partial U_{z,0}}{\partial Y}A_{yz,0}, \tag{3.11g}$$

and

$$\mathcal{S}_{yz,0} = -U_{z,0}\frac{\partial A_{yz,0}}{\partial Z} - U_{y,0}\frac{\partial A_{yz,0}}{\partial Y} + \frac{\partial U_{z,0}}{\partial Y}A_{yy,0}, \tag{3.11h}$$

where we have used (3.3*d*) to simplify (3.11*d*), (3.11*f*), (3.11*g*) and (3.11*h*).

These governing equations are supplemented by the boundary conditions

$$U_{z,1}(H(Z), Z) = 0, \quad U_{y,1}(H(Z), Z) = 0, \quad \frac{\partial U_{z,1}}{\partial Y}(0, Z) = 0, \quad \int_0^{H(Z)} U_{z,1}(Y, Z)\,\mathrm{d}Y = 0. \tag{3.12a–d}$$

The last term on the right-hand side of (3.11*b*) solely depends on the leading-order solution, and thus can be explicitly calculated using (3.7), (3.8) and (3.9*a*,*b*) to yield

$$\tilde{\beta}\left[\frac{\partial \mathcal{S}_{zz,0}}{\partial Z} + \frac{\partial \mathcal{S}_{yz,0}}{\partial Y}\right] = -\frac{18\tilde{\beta}}{H(Z)^5}\frac{\mathrm{d}H(Z)}{\mathrm{d}Z} = \frac{9\tilde{\beta}}{2}\frac{\mathrm{d}}{\mathrm{d}Z}\left(\frac{1}{H(Z)^4}\right). \tag{3.13}$$

Next, integrating (3.11*b*) twice with respect to Y, using (3.13), and applying the boundary conditions (3.12*a*) and (3.12*c*), we obtain

$$U_{z,1}(Y, Z) = \frac{1}{2}\frac{\mathrm{d}}{\mathrm{d}Z}\left(P_1 - \frac{9}{2}\frac{\tilde{\beta}}{H(Z)^4}\right)(Y^2 - H(Z)^2). \tag{3.14}$$

To determine $\mathrm{d}P_1/\mathrm{d}Z$, we use the integral constraint (3.12*d*) to find

$$\frac{\mathrm{d}P_1}{\mathrm{d}Z} = -\frac{18\tilde{\beta}}{H(Z)^5}\frac{\mathrm{d}H(Z)}{\mathrm{d}Z} = \frac{9}{2}\tilde{\beta}\frac{\mathrm{d}}{\mathrm{d}Z}\left(\frac{1}{H(Z)^4}\right), \tag{3.15}$$

and, thus, $U_{z,1} \equiv 0$. From the continuity equation (3.11*a*), it then follows that $U_{y,1} \equiv 0$.

Integrating (3.15) with respect to Z from 0 to 1 provides the pressure drop at $O(De)$,

$$\Delta P_1 = \frac{9}{2}\tilde{\beta}\left(\frac{1}{H(0)^4} - \frac{1}{H(1)^4}\right) = \frac{9}{2}\tilde{\beta}\left(\frac{H(1)^4 - H(0)^4}{H(0)^4 H(1)^4}\right). \tag{3.16}$$

From (3.16), it follows that ΔP_1 may increase, decrease or not change the total pressure drop of the Oldroyd-B fluid, depending on the geometry. Specifically, (3.16) indicates that the non-dimensional pressure drop at the first order solely depends on the difference in channel height at the inlet and outlet rather than on details of the shape. For $H(1) > H(0)$, the first-order correction leads to an increase in the pressure drop, for $H(1) < H(0)$ to a decrease in the pressure drop, and for $H(1) = H(0)$ there is no contribution to the pressure drop that is first order in De. Such an increase (decrease) in the pressure drop for $H(1) > H(0)$ ($H(1) < H(0)$) is consistent with 2-D numerical simulations using the Oldroyd-B model for expanding (contracting) channels (Binding *et al.* 2006; Varchanis *et al.* 2022).

We note that to first order in De our governing equations for the Oldroyd-B model, in the case of $\tilde{\beta} = 1$ that corresponds to the UCM model, are the same as the governing equations of the second-order fluid with a vanishing second normal stress difference coefficient. For example, our expressions (3.11*g*) and (3.11*h*) for $\mathcal{S}_{zz,0}$ and $\mathcal{S}_{yz,0}$ are identical to the corresponding relations given in Boyko & Stone (2021) for the second-order fluid in the case of the vanishing second normal stress difference coefficient. Therefore, unsurprisingly, the velocity field remains Newtonian at $O(De)$, i.e. $U_{z,1} = U_{y,1} = 0$, following the theorem of Tanner and Pipkin (Tanner 1966; Tanner & Pipkin 1969), which is an extension of Giesekus' earlier work (Giesekus 1963).

As the velocity components vanish at the first order, the components of the conformation tensor at this order can be calculated using the leading-order velocity field,

$$A_{zz,1} = \frac{18Y^2}{H(Z)^6}, \tag{3.17a}$$

$$A_{yz,1} = 18\frac{\mathrm{d}H(Z)}{\mathrm{d}Z}\frac{Y(H(Z)^2 - 2Y^2)}{H(Z)^7}, \tag{3.17b}$$

$$A_{yy,1} = \frac{9}{2}\frac{4(-2Y^2 + H(Z)^2)^2 H'(Z)^2 - H(Z)H''(Z)(Y^2 - H(Z)^2)^2}{H(Z)^8}, \tag{3.17c}$$

where primes indicate derivatives with respect to Z.

3.3. *Second-order solution*

At the second order, $O(De^2)$, the governing equations (2.14)–(2.15) take the form

$$\frac{\partial U_{z,2}}{\partial Z} + \frac{\partial U_{y,2}}{\partial Y} = 0, \tag{3.18a}$$

$$\frac{\mathrm{d}P_2}{\mathrm{d}Z} = \frac{\partial^2 U_{z,2}}{\partial Y^2} + \tilde{\beta}\left[\frac{\partial \mathcal{S}_{zz,1}}{\partial Z} + \frac{\partial \mathcal{S}_{yz,1}}{\partial Y}\right], \tag{3.18b}$$

$$\frac{\partial P_2}{\partial Y} = 0, \tag{3.18c}$$

$$U_{z,0}\frac{\partial A_{zz,1}}{\partial Z} + U_{y,0}\frac{\partial A_{zz,1}}{\partial Y} - 2\frac{\partial U_{z,0}}{\partial Z}A_{zz,1} - 2\frac{\partial U_{z,0}}{\partial Y}A_{yz,1} = -A_{zz,2}, \tag{3.18d}$$

$$U_{z,0}\frac{\partial A_{yy,1}}{\partial Z} + U_{y,0}\frac{\partial A_{yy,1}}{\partial Y} - 2\frac{\partial U_{y,0}}{\partial Z}A_{yz,1} - 2\frac{\partial U_{y,0}}{\partial Y}A_{yy,1} - 2\frac{\partial U_{y,2}}{\partial Y} = -A_{yy,2}, \tag{3.18e}$$

$$U_{z,0}\frac{\partial A_{yz,1}}{\partial Z} + U_{y,0}\frac{\partial A_{yz,1}}{\partial Y} - \frac{\partial U_{y,0}}{\partial Z}A_{zz,1} - \frac{\partial U_{z,0}}{\partial Y}A_{yy,1} - \frac{\partial U_{z,2}}{\partial Y} = -A_{yz,2}, \tag{3.18f}$$

$$\mathcal{S}_{zz,1} = -U_{z,0}\frac{\partial A_{zz,1}}{\partial Z} - U_{y,0}\frac{\partial A_{zz,1}}{\partial Y} + 2\frac{\partial U_{z,0}}{\partial Z}A_{zz,1} + 2\frac{\partial U_{z,0}}{\partial Y}A_{yz,1}, \tag{3.18g}$$

$$\mathcal{S}_{yz,1} = -U_{z,0}\frac{\partial A_{yz,1}}{\partial Z} - U_{y,0}\frac{\partial A_{yz,1}}{\partial Y} + \frac{\partial U_{y,0}}{\partial Z}A_{zz,1} + \frac{\partial U_{z,0}}{\partial Y}A_{yy,1}, \tag{3.18h}$$

where we have used the fact that $U_{z,1} \equiv 0$ and $U_{y,1} \equiv 0$. The governing equations (3.18) are supplemented by the boundary conditions

$$U_{z,2}(H(Z), Z) = 0, \quad U_{y,2}(H(Z), Z) = 0, \quad \frac{\partial U_{z,2}}{\partial Y}(0, Z) = 0, \quad \int_0^{H(Z)} U_{z,2}(Y, Z)\,\mathrm{d}Y = 0. \tag{3.19a–d}$$

The last term on the right-hand side of (3.18*b*) solely depends on the leading- and first-order solutions, and thus can be calculated using (3.18*g*)–(3.18*h*),

$$\tilde{\beta}\left[\frac{\partial \mathcal{S}_{zz,1}}{\partial Z} + \frac{\partial \mathcal{S}_{yz,1}}{\partial Y}\right] = \frac{81\tilde{\beta}}{2}\frac{\left(Y^2 - H(Z)^2\right)\left[4H(Z)H'(Z)^2 + H''(Z)\left(Y^2 - H(Z)^2\right)\right]}{H(Z)^{10}}. \tag{3.20}$$

Integrating (3.18*b*) twice with respect to Y, using (3.20), and applying the boundary conditions (3.19*a*) and (3.19*c*), we obtain

$$U_{z,2} = (Y^2 - H^2)\left(\frac{1}{2}\frac{\mathrm{d}P_2}{\mathrm{d}Z} - \frac{27\tilde{\beta}}{20}\frac{10HH'^2\left(Y^2 - 5H^2\right) + H''\left(Y^4 - 4(YH)^2 + 11H^4\right)}{H^{10}}\right). \tag{3.21}$$

To determine $\mathrm{d}P_2/\mathrm{d}Z$, we use the integral constraint (3.19*d*), to find

$$\frac{\mathrm{d}P_2}{\mathrm{d}Z} = -\frac{324}{35}\tilde{\beta}\left(\frac{14H'(Z)^2}{H(Z)^7} - \frac{3H''(Z)}{H(Z)^6}\right). \tag{3.22}$$

Integrating (3.22) with respect to Z from 0 to 1 yields the pressure drop at $O(De^2)$,

$$\Delta P_2 = \frac{324}{35}\tilde{\beta}\int_0^1 \left(\frac{14H'(Z)^2}{H(Z)^7} - \frac{3H''(Z)}{H(Z)^6}\right)\mathrm{d}Z. \tag{3.23}$$

For a given flow rate q, we have determined the dimensionless pressure drop $\Delta P = \Delta p/(\eta_0 q\ell/2h_\ell^3)$ as a function of the shape function $H(Z)$, the viscosity ratio $\tilde{\beta}$ and the Deborah number De,

$$\Delta P = \Delta P_0(H(Z)) + De\,\Delta P_1(\tilde{\beta}, H(Z)) + De^2\Delta P_2(\tilde{\beta}, H(Z)) + O(\epsilon^2, De^3), \tag{3.24}$$

where the expressions for ΔP_0, ΔP_1 and ΔP_2 are given in (3.10), (3.16) and (3.23), respectively.

We note that once $U_{z,2}(Y,Z)$ is determined from (3.21) and (3.22), $U_{y,2}(Y,Z)$ can be found using the continuity (3.18*a*) and (3.19*b*). Furthermore, the components of the conformation tensor at this order can be calculated from (3.18*d*)–(3.18*f*). Although the resulting expressions are readily found using MATHEMATICA, they are rather lengthy and, thus, not presented here.

4. Reciprocal theorem for the flow of an Oldroyd-B fluid in narrow geometries

In this section, we exploit the reciprocal theorem for complex fluids in narrow geometries, recently derived by Boyko & Stone (2021), to calculate the flow rate–pressure drop relation, bypassing the detailed calculations of the viscoelastic flow problem. In particular, we show that the reciprocal theorem allows one to obtain the q–Δp relation at the next order, $O(De^3)$, relying only on the solutions from previous orders. For completeness, we present the governing equations and the key relations derived in Boyko & Stone (2021), adapted to the notation in this paper.

Let $\hat{\boldsymbol{u}}$ and $\hat{\boldsymbol{\sigma}}$ denote the velocity and stress fields, respectively, corresponding to the solution of the Stokes equations in the same domain with the constant viscosity η_0. The corresponding governing equations are

$$\boldsymbol{\nabla}\cdot\hat{\boldsymbol{u}} = 0, \quad \boldsymbol{\nabla}\cdot\hat{\boldsymbol{\sigma}} = \boldsymbol{0} \quad \text{with } \hat{\boldsymbol{\sigma}} = -\hat{p}\boldsymbol{I} + 2\eta_0\hat{\boldsymbol{E}}. \tag{4.1a,b}$$

The reciprocal theorem states that two flows $(\boldsymbol{u}, \boldsymbol{\sigma})$ and $(\hat{\boldsymbol{u}}, \hat{\boldsymbol{\sigma}})$, governed by (2.8) and (4.1), satisfy (see Boyko & Stone 2021),

$$\int_{S_0} \boldsymbol{n}\cdot\boldsymbol{\sigma}\cdot\hat{\boldsymbol{u}}\,\mathrm{d}S + \int_{S_\ell} \boldsymbol{n}\cdot\boldsymbol{\sigma}\cdot\hat{\boldsymbol{u}}\,\mathrm{d}S - \int_{S_0} \boldsymbol{n}\cdot\hat{\boldsymbol{\sigma}}\cdot\boldsymbol{u}\,\mathrm{d}S - \int_{S_\ell} \boldsymbol{n}\cdot\hat{\boldsymbol{\sigma}}\cdot\boldsymbol{u}\,\mathrm{d}S = \eta_p\int_{\mathcal{V}} \boldsymbol{S}:\hat{\boldsymbol{E}}\,\mathrm{d}\mathcal{V}, \tag{4.2}$$

where $\mathcal{V}$ is the entire fluid volume bounded by the surface of the top and bottom walls S_w, and the surfaces at the inlet and outlet S_0 and S_ℓ at $z = 0$ and $z = \ell$, respectively, and $\boldsymbol{n}$ is

the unit outward normal to $S_{0,\ell}$. Note that the integrals over the walls S_w vanish because there $\boldsymbol{u} = \hat{\boldsymbol{u}} = \boldsymbol{0}$.

Using the scaling analysis and (2.6), (2.10) and (4.1*a*,*b*), the terms $\eta_p \boldsymbol{S} : \hat{\boldsymbol{E}}$, $\boldsymbol{n} \cdot \boldsymbol{\sigma} \cdot \hat{\boldsymbol{u}}$, and $\boldsymbol{n} \cdot \hat{\boldsymbol{\sigma}} \cdot \boldsymbol{u}$, appearing in (4.2), are approximately:

$$\eta_p \boldsymbol{S} : \hat{\boldsymbol{E}} = \frac{\eta_p De u_c^2}{h_\ell^2} \left(\mathcal{S}_{zz} \frac{\partial \hat{U}_z}{\partial Z} + \mathcal{S}_{yz} \frac{\partial \hat{U}_z}{\partial Y} + O(\epsilon^2) \right), \tag{4.3a}$$

$$\boldsymbol{n} \cdot \boldsymbol{\sigma} \cdot \hat{\boldsymbol{u}} = \mp \frac{\eta_0 u_c^2 \ell}{h_\ell^2} [(-P + \tilde{\beta} De \mathcal{S}_{zz}) \hat{U}_z + O(\epsilon^2)]_{Z=0,1}, \tag{4.3b}$$

$$\boldsymbol{n} \cdot \hat{\boldsymbol{\sigma}} \cdot \boldsymbol{u} = \mp \frac{\eta_0 u_c^2 \ell}{h_\ell^2} [-\hat{P} U_z + O(\epsilon^2)]_{Z=0,1}, \tag{4.3c}$$

where the minus sign in (4.3*b*) and (4.3*c*) corresponds to S_0 and the plus sign corresponds to S_ℓ. Substituting (4.3) into (4.2), we obtain

$$\begin{aligned} &\int_0^{H(0)} [(P - \tilde{\beta} De \mathcal{S}_{zz}) \hat{U}_z - \hat{P} U_z]_{Z=0} \, \mathrm{d}Y - \int_0^{H(1)} [(P - \tilde{\beta} De \mathcal{S}_{zz}) \hat{U}_z - \hat{P} U_z]_{Z=1} \, \mathrm{d}Y \\ &\quad = \tilde{\beta} De \int_0^1 \int_0^{H(Z)} \left(\mathcal{S}_{zz} \frac{\partial \hat{U}_z}{\partial Z} + \mathcal{S}_{yz} \frac{\partial \hat{U}_z}{\partial Y} \right) \mathrm{d}Y \mathrm{d}Z + O(\epsilon^2), \end{aligned} \tag{4.4}$$

where $H(Z)$ is the non-dimensional shape of the channel. Noting that $P = P(Z) + O(\epsilon^2)$, $\hat{P} = \hat{P}(Z) + O(\epsilon^2)$ and $\int_0^{H(Z)} U_z \, \mathrm{d}Y = \int_0^{H(Z)} \hat{U}_z \, \mathrm{d}Y = 1$, and defining $\Delta P = P(0) - P(1)$ and $\Delta \hat{P} = \hat{P}(0) - \hat{P}(1)$, (4.4) simplifies to

$$\begin{aligned} \Delta P = \Delta \hat{P} &+ \tilde{\beta} De \int_0^{H(0)} [\mathcal{S}_{zz} \hat{U}_z]_{Z=0} \, \mathrm{d}Y - \tilde{\beta} De \int_0^{H(1)} [\mathcal{S}_{zz} \hat{U}_z]_{Z=1} \, \mathrm{d}Y \\ &+ \tilde{\beta} De \int_0^1 \int_0^{H(Z)} \left(\mathcal{S}_{zz} \frac{\partial \hat{U}_z}{\partial Z} + \mathcal{S}_{yz} \frac{\partial \hat{U}_z}{\partial Y} \right) \mathrm{d}Y \, \mathrm{d}Z + O(\epsilon^2), \end{aligned} \tag{4.5}$$

where the solution of the corresponding Newtonian problem is obtained from (3.7), (3.8) and (3.10) as

$$\Delta \hat{P} = 3 \int_0^1 \frac{\mathrm{d}Z}{H(Z)^3}, \quad \hat{U}_z = \frac{3}{2} \frac{H(Z)^2 - Y^2}{H(Z)^3}, \quad \hat{U}_y = \frac{3}{2} \frac{\mathrm{d}H(Z)}{\mathrm{d}Z} \frac{Y(H(Z)^2 - Y^2)}{H(Z)^4}. \tag{4.6a–c}$$

Equation (4.5) indicates that the dimensionless pressure drop of the viscoelastic flow of an Oldroyd-B fluid in a narrow channel consists of four contributions. The first term on the right-hand side of (4.5) represents the Newtonian contribution to the pressure drop. The second and third terms represent the contribution of the viscoelastic normal stress of the complex fluid at the inlet and outlet of the channel. Finally, the last term represents the viscoelastic contribution due to elongational ($\mathcal{S}_{zz} \partial \hat{U}_z / \partial Z$) and shearing ($\mathcal{S}_{yz} \partial \hat{U}_z / \partial Y$) effects within the fluid domain $\mathcal{V}$.

Furthermore, (4.5) clearly shows that the dimensionless pressure drop depends on the $\mathcal{S}_{zz}$ and $\mathcal{S}_{yz}$, and thus, generally, requires the solution of the nonlinear viscoelastic problem. However, in the weakly viscoelastic limit, corresponding to $De \ll 1$, the reciprocal

theorem (4.5) allows one to determine the pressure drop at the current order only with the knowledge of the solution of the Newtonian problem and previous orders. For example, we can determine ΔP_1 with the knowledge of the solution of the Newtonian problem and the leading-order solution. Similarly, we can determine ΔP_2 with the knowledge of the solution of the Newtonian problem and the leading- and first-order solutions of the viscoelastic problem. We note that our analysis assumes only negligible fluid inertia, a shallow geometry, $\epsilon \ll 1$, and the weakly viscoelastic limit, $De \ll 1$, while allowing Wi to be $O(1)$.

In the next sections, we illustrate the use of the reciprocal theorem (4.5) and provide closed-form analytical expressions for the dimensionless pressure drop of an Oldroyd-B fluid up to $O(De^3)$ for 2-D geometries.

4.1. *Expression for the dimensionless pressure drop at the first order*

Substituting (3.1) into (4.5) and considering the first order, $O(De)$, we obtain

$$\Delta P_1 = \tilde{\beta}\int_0^{H(0)} [\mathcal{S}_{zz,0}\hat{U}_z]_{Z=0}\,\mathrm{d}Y - \tilde{\beta}\int_0^{H(1)} [\mathcal{S}_{zz,0}\hat{U}_z]_{Z=1}\,\mathrm{d}Y + \tilde{\beta}\int_0^1\int_0^{H(Z)} \left(\mathcal{S}_{zz,0}\frac{\partial \hat{U}_z}{\partial Z} + \mathcal{S}_{yz,0}\frac{\partial \hat{U}_z}{\partial Y}\right)\mathrm{d}Y\,\mathrm{d}Z. \tag{4.7}$$

Equation (4.7) indicates that the first-order pressure drop ΔP_1 can be calculated with the knowledge of the solutions of the Newtonian problem and the leading-order viscoelastic problem. Using the expressions for $\mathcal{S}_{zz,0}$ and $\mathcal{S}_{yz,0}$, given in (3.11*g*) and (3.11*h*), we obtain

$$\Delta P_1 = \frac{18}{5}\tilde{\beta}\left(\frac{1}{H(0)^4} - \frac{1}{H(1)^4}\right) + \frac{9}{10}\tilde{\beta}\left(\frac{1}{H(0)^4} - \frac{1}{H(1)^4}\right) = \frac{9}{2}\tilde{\beta}\left(\frac{1}{H(0)^4} - \frac{1}{H(1)^4}\right), \tag{4.8}$$

which is exactly (3.16).

4.2. *Expression for the dimensionless pressure drop at the second order*

At the second order, $O(De^2)$, we have

$$\Delta P_2 = \tilde{\beta}\int_0^{H(0)} [\mathcal{S}_{zz,1}\hat{U}_z]_{Z=0}\,\mathrm{d}Y - \tilde{\beta}\int_0^{H(1)} [\mathcal{S}_{zz,1}\hat{U}_z]_{Z=1}\,\mathrm{d}Y + \tilde{\beta}\int_0^1\int_0^{H(Z)} \left(\mathcal{S}_{zz,1}\frac{\partial \hat{U}_z}{\partial Z} + \mathcal{S}_{yz,1}\frac{\partial \hat{U}_z}{\partial Y}\right)\mathrm{d}Y\,\mathrm{d}Z. \tag{4.9}$$

The second-order pressure drop ΔP_2 solely depends on the solution of the Newtonian problem and the leading- and first-order viscoelastic problems. Using the expressions for $\mathcal{S}_{zz,1}$ and $\mathcal{S}_{yz,1}$, given in (3.18*g*) and (3.18*h*), and (4.6*b*), we obtain

$$\Delta P_2 = \frac{648}{35}\tilde{\beta}\left(\frac{H'(0)}{H(0)^6} - \frac{H'(1)}{H(1)^6}\right) + \frac{324}{35}\tilde{\beta}\int_0^1 \left(\frac{2H'(Z)^2}{H(Z)^7} - \frac{H''(Z)}{H(Z)^6}\right)\mathrm{d}Z, \tag{4.10}$$

which can be rewritten as

$$\Delta P_2 = \frac{324}{35}\tilde{\beta}\int_0^1 \left[\frac{14H'(Z)^2}{H(Z)^7} - \frac{3H''(Z)}{H(Z)^6}\right] \mathrm{d}Z, \tag{4.11}$$

giving exactly (3.23).

4.3. *Expression for the dimensionless pressure drop at the third order*

At the third order, $O(De^3)$, (4.5) takes the form

$$\begin{aligned}\Delta P_3 = {} & \tilde{\beta}\int_0^{H(0)} [\mathcal{S}_{zz,2}\hat{U}_z]_{Z=0}\,\mathrm{d}Y - \tilde{\beta}\int_0^{H(1)} [\mathcal{S}_{zz,2}\hat{U}_z]_{Z=1}\,\mathrm{d}Y \\ & + \tilde{\beta}\int_0^1\int_0^{H(Z)} \left(\mathcal{S}_{zz,2}\frac{\partial \hat{U}_z}{\partial Z} + \mathcal{S}_{yz,2}\frac{\partial \hat{U}_z}{\partial Y}\right) \mathrm{d}Y\,\mathrm{d}Z,\end{aligned} \tag{4.12}$$

where $\mathcal{S}_{zz,2}$ and $\mathcal{S}_{yz,2}$ are given by

$$\mathcal{S}_{zz,2} = -U_{z,0}\frac{\partial A_{zz,2}}{\partial Z} - U_{y,0}\frac{\partial A_{zz,2}}{\partial Y} + 2\frac{\partial U_{z,0}}{\partial Z}A_{zz,2} + 2\frac{\partial U_{z,0}}{\partial Y}A_{yz,2} + 2\frac{\partial U_{z,2}}{\partial Y}A_{yz,0}, \tag{4.13a}$$

$$\begin{aligned}\mathcal{S}_{yz,2} = {} & -U_{z,0}\frac{\partial A_{yz,2}}{\partial Z} - U_{z,2}\frac{\partial A_{yz,0}}{\partial Z} - U_{y,0}\frac{\partial A_{yz,2}}{\partial Y} \\ & - U_{y,2}\frac{\partial A_{yz,0}}{\partial Y} + \frac{\partial U_{y,0}}{\partial Z}A_{zz,2} + \frac{\partial U_{z,0}}{\partial Y}A_{yy,2} + \frac{\partial U_{z,2}}{\partial Y}A_{yy,0}.\end{aligned} \tag{4.13b}$$

As $\mathcal{S}_{zz,2}$ and $\mathcal{S}_{yz,2}$ depend on the solution from previous orders, we can calculate the third-order pressure drop ΔP_3 using the solution of the Newtonian problem and the solution of the leading-, first- and second-order viscoelastic problems.

The resulting expression for ΔP_3 is

$$\Delta P_3 = \frac{648\tilde{\beta}(9-\tilde{\beta})}{35}\left(\frac{H'(0)^2}{H(0)^8} - \frac{H'(1)^2}{H(1)^8}\right) - \frac{216\tilde{\beta}(8-\tilde{\beta})}{35}\left(\frac{H''(0)}{H(0)^7} - \frac{H''(1)}{H(1)^7}\right). \tag{4.14}$$

In summary, using the reciprocal theorem (4.5) we have determined the dimensionless pressure drop $\Delta P = \Delta p/(\eta_0 q\ell/2h_\ell^3)$ as a function of the shape function $H(Z)$, the viscosity ratio $\tilde{\beta}$ and the Deborah number De up to $O(De^3)$,

$$\Delta P = \Delta P_0 + De\Delta P_1 + De^2\Delta P_2 + De^3\Delta P_3 + O(\epsilon^2, De^4), \tag{4.15}$$

where the expressions for ΔP_0, ΔP_1, ΔP_2 and ΔP_3 are given in (3.10), (4.8), (4.11) and (4.14), respectively. We note that, physically, $\Delta P = \Delta p/(\eta_0 q\ell/2h_\ell^3)$ represents the dimensionless hydrodynamic resistance $(\Delta p/q)$. The reader is reminded that the expression for the non-dimensional pressure drop (4.15) applies to the geometry shown in figure 1, where the entrance and exit effects are eliminated. When a viscoelastic fluid exits from the non-uniform region directly to the atmosphere or a large reservoir, significant exit effects can arise due to axial stresses, thus requiring a correction to be added to (4.15).

5. Results and comparison with finite-element simulations

In this section, we present the analytical results for the pressure drop and flow and stress fields of the Oldroyd-B fluid developed in §§ 3 and 4. We also validate the predictions of our theoretical model by performing 2-D numerical simulations with the finite-element software COMSOL Multiphysics (version 5.6, COMSOL AB, Stockholm, Sweden), with which we compare our analytical results. The details of the numerical procedure are provided in Appendix A.

As an illustrative example, we specifically consider the case of a hyperbolic contracting channel of the form

$$H(Z) = \frac{\alpha}{(\alpha - 1)Z + 1}, \tag{5.1}$$

where $\alpha = h_0/h_\ell$ is a ratio of the heights at the inlet and outlet; for the contracting geometry we have $\alpha > 1$. For the 2-D hyperbolic contracting geometry (5.1), closed-form analytical expressions for the contributions to the pressure drop up to $O(De^3)$ are obtained from (3.10), (4.8), (4.11) and (4.14) as

$$\Delta P_0 = \frac{3}{4}\frac{(1+\alpha)(1+\alpha^2)}{\alpha^3}, \tag{5.2a}$$

$$\Delta P_1 = \frac{9}{2}\tilde{\beta}\frac{1-\alpha^4}{\alpha^4}, \tag{5.2b}$$

$$\Delta P_2 = \frac{648}{35}\tilde{\beta}\frac{(1+\alpha)(1+\alpha^2)(1-\alpha)^2}{\alpha^5}, \tag{5.2c}$$

$$\Delta P_3 = \frac{216}{35}\tilde{\beta}(11-\tilde{\beta})\frac{(1+\alpha)(1+\alpha^2)(1-\alpha)^3}{\alpha^6}. \tag{5.2d}$$

As expected, (5.2) clearly shows that for the straight channel, $\alpha = 1$, the ΔP_1, ΔP_2 and ΔP_3 contributions vanish and the pressure drop of the Oldroyd-B fluid is identical to the pressure drop of the Newtonian fluid with the same zero-shear-rate viscosity.

5.1. *Variation of pressure drop with the Deborah and Weissenberg numbers*

In this work, we mainly present the results for the Oldroyd-B fluid with $\tilde{\beta} = 0.4$ in two hyperbolic geometries, which have an identical inlet-to-outlet ratio $\alpha = 4$ but different aspect ratios $\epsilon = h_\ell/\ell$. The first geometry we consider has $\epsilon = 0.02$, for which the assumptions of the lubrication approximation are expected to be well satisfied. In addition, aiming to examine the pressure drop in less narrow configurations, the second geometry we study corresponds to $\epsilon = 0.1$. For such geometry, even if $\epsilon = 0.1$ can be considered a small parameter, the requirement $\alpha\epsilon \ll 1$, representing the slow variation assumption in the lubrication theory, is not satisfied because $\alpha\epsilon = 0.4$ is $O(1)$. However, as we show in the following, although the lubrication assumptions are not strictly satisfied in this case, our theory captures fairly well the variation of the pressure drop with De.

We present the non-dimensional pressure drop $\Delta P = \Delta p/(\eta_0 q\ell/2h_\ell^3)$ as a function of $De = \lambda q/(2\ell h_\ell)$ (or $Wi = \lambda q/(2h_\ell^2)$) in figure 2(*a*,*b*) for the Oldroyd-B fluid in a hyperbolic contracting channel for $\epsilon = 0.02$ (*a*) and $\epsilon = 0.1$ (*b*), with $\alpha = 4$ and $\tilde{\beta} = 0.4$. Dotted lines represent the first-order asymptotic solution, given by (5.2*a*)–(5.2*b*), solid lines represent the second-order asymptotic solution, given by (5.2*a*)–(5.2*c*), and dashed lines represent the third-order asymptotic solution, given by (5.2*a*)–(5.2*d*). Black triangles

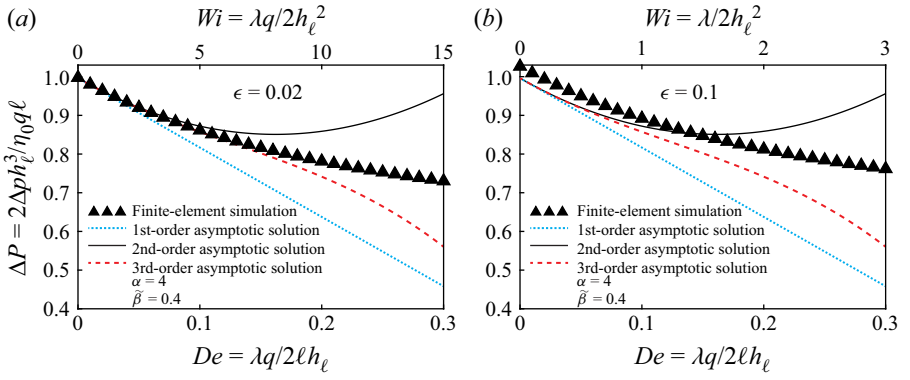

Figure 2. Non-dimensional pressure drop for the Oldroyd-B fluid in a hyperbolic contracting channel described by (5.1). (*a*, *b*) Dimensionless pressure drop $\Delta P = \Delta p/(\eta_0 q\ell/2h_\ell^3)$ as a function of $De = \lambda q/(2\ell h_\ell)$ (or $Wi = \lambda q/(2h_\ell^2)$) for (*a*) $\epsilon = 0.02$ and (*b*) $\epsilon = 0.1$. Black triangles (▲) represent the results of the finite-element simulation. Dotted lines represent the first-order asymptotic solution, given by (5.2*a*)–(5.2*b*). Solid lines represent the second-order asymptotic solution, given by (5.2*a*)–(5.2*c*). Dashed lines represent the third-order asymptotic solution, given by (5.2*a*)–(5.2*d*). All calculations were performed using $\alpha = 4$ and $\tilde{\beta} = 0.4$.

represent the results of the numerical simulation obtained from calculating the pressure drop along the centreline ($Y = 0$). We note that while our analysis assumes $De \ll 1$, where Deborah number is the product of the relaxation time and the characteristic extensional rate of the flow, the Weissenberg number *Wi*, which is the product of the relaxation time and the characteristic shear rate of the flow, is $O(1)$ (see also Ahmed & Biancofiore 2021). To further highlight this point, we present our results both as a function of *De* and *Wi*.

Similar to previous numerical reports using the Oldroyd-B model for studying the flow of Boger fluids in 2-D abruptly contracting geometries (see, e.g., Aboubacar *et al.* 2002; Alves *et al.* 2003; Binding *et al.* 2006; Aguayo *et al.* 2008), our high-order analytical and numerical simulations in figures 2(*a*) and 2(*b*) predict a monotonic decrease in the pressure drop with increasing *De* (or *Wi*). In addition, the results in figure 2(*a*) clearly show that accounting for higher orders of the analytical solutions for the pressure drop significantly improves the agreement with the numerical simulation results for $\epsilon = 0.02$, yielding a relative error of approximately 5 % for up to $De = 0.2$, corresponding to $Wi = 10$. For the case of $\epsilon = 0.1$, shown in figure 2(*b*), the third-order asymptotic solution, given by (5.2*a*)–(5.2*d*), slightly underpredicts the pressure drop, yet even for $De = 0.2$, corresponding to $Wi = 2$, it results in a modest relative error of approximately 9 %. Furthermore, it follows from figure 2(*b*) that, for $\epsilon = 0.1$, a small discrepancy between analytical solutions and numerical simulations exists even for the Newtonian case ($De = 0$), thus indicating that the error is due to the non-fulfillment of the lubrication assumptions rather than the low-*De* analysis.

5.2. *Assessing the effect of different contributions to the pressure drop*

The results presented in the previous subsection predict a reduction in the dimensionless pressure drop with increasing *De* or *Wi* for the Oldroyd-B fluid in a hyperbolic contracting channel. In this subsection, to provide insight into the source of such a reduction, we elucidate the relative importance of different contributions to the pressure drop using our analytical predictions and numerical simulations. To this end, we integrate the momentum

equation (2.14*b*) with respect to Z from 0 to 1 along the centreline ($Y = 0$) and obtain the dimensionless pressure drop,

$$\Delta P = \underbrace{\epsilon^2 \left[\left.\frac{\partial U_z}{\partial Z}\right|_{Y=0,Z=0} - \left.\frac{\partial U_z}{\partial Z}\right|_{Y=0,\,Z=1} \right]}_{①} + \underbrace{\int_1^0 \left.\frac{\partial^2 U_z}{\partial Y^2}\right|_{Y=0} \mathrm{d}Z}_{②}$$
$$+ \underbrace{\tilde{\beta} De \Delta \mathcal{S}_{zz}}_{③} + \underbrace{\tilde{\beta} De \int_1^0 \left.\frac{\partial \mathcal{S}_{yz}}{\partial Y}\right|_{Y=0} \mathrm{d}Z}_{④}, \tag{5.3}$$

where $\Delta P = P(0,0) - P(0,1)$ and $\Delta \mathcal{S}_{zz} = \mathcal{S}_{zz}(0,0) - \mathcal{S}_{zz}(0,1)$. We note that for a general geometry the axial pressure drop may strongly depend on the Y coordinate along which it is evaluated. However, as for narrow geometries $P = P(Z) + O(\epsilon^2)$, i.e. the pressure is independent of Y up to $O(\epsilon^2)$, we expect the results to be weakly dependent on the value of Y along which the integration over Z is performed.

Equation (5.3) clearly shows that the pressure drop of viscoelastic flow of consists of four contributions. The first (①) and third (③) terms on the right-hand side of (5.3) represent the contribution of the Newtonian and viscoelastic viscous axial stress differences, respectively. The second (②) and fourth (④) terms represent, respectively, the contribution of the Newtonian and viscoelastic viscous shear stresses. As the first term, ①, scales as $O(\epsilon^2)$, we expect it to be negligible for narrow geometries under consideration.

The different contributions to the non-dimensional pressure drop as a function of De (or Wi) are shown in figures 3(*a*) and 3(*b*) for $\epsilon = 0.02$ (*a*) and $\epsilon = 0.1$ (*b*), with $\alpha = 4$ and $\tilde{\beta} = 0.4$. Dots, triangles, crosses and circles, respectively, represent the contributions ①–④ extracted from numerical simulations. Black solid, purple solid, cyan dotted and grey dash-dotted lines represent the ①–④ contributions obtained from the asymptotic solution up to $O(De^2)$. Red dashed lines represent the analytically obtained contribution ④ up to $O(De^3)$.

First, as expected, both our analytical and numerical simulations show that the ① term has a negligible contribution to the pressure drop. Second, somewhat surprisingly, from figure 3(*a*, *b*) it follows that the ③ term, representing the viscoelastic viscous axial stress difference along the centreline, also has a negligible contribution to the pressure drop. We rationalise the latter by noting that, for convenience, we have calculated the pressure drop along the centreline, and for $Y = 0$, the viscoelastic viscous axial stress difference is indeed negligible. However, because the pressure is independent of Y to $O(\epsilon^2)$, (2.14*b*) can be integrated with respect to Z from 0 to 1, while setting the different values of Y, for which the viscoelastic viscous axial stress difference may have an apparent contribution to the pressure drop (see figure 4).

It is evident from figures 3(*a*) and 3(*b*) that only the ② and ④ terms, which are associated with the Newtonian and viscoelastic viscous shear stresses, have a significant contribution to the pressure drop, calculated along $Y = 0$. The ② term shows only a weak dependence on De and has approximately a constant value, corresponding to the Newtonian case. Such a weak dependence on De is expected, since ② is related to the velocity $U_z = U_{z,0} + De^2 U_{z,2} + O(De^3, \epsilon^2)$, which has only $O(De^2)$ and higher contributions. We observe an excellent agreement between our analytical predictions and the results of the numerical simulations for ② in the case $\epsilon = 0.02$ throughout the investigated range of De number. Moreover, although for $\epsilon = 0.1$ the lubrication

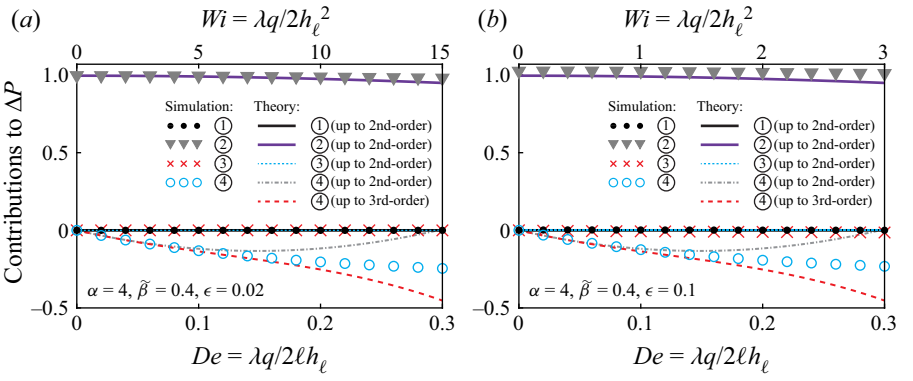

Figure 3. Contributions to the non-dimensional pressure drop of the Oldroyd-B fluid in a hyperbolic contracting channel. (*a*, *b*) Different contributions to the dimensionless pressure drop as a function of $De = \lambda q/(2\ell h_\ell)$ (or $Wi = \lambda q/(2h_\ell^2)$) for (*a*) $\epsilon = 0.02$ and (*b*) $\epsilon = 0.1$. Dots, triangles, crosses and circles represent the ①–④ contributions extracted from 2-D numerical simulations. Black solid, purple solid, cyan dotted, and grey dash-dotted lines represent the ①–④ contributions obtained from the asymptotic solution up to $O(De^2)$. Red dashed lines represent the analytically obtained ④ contribution up to $O(De^3)$. All calculations were performed using $\alpha = 4$ and $\tilde{\beta} = 0.4$.

assumptions are not strictly satisfied, our asymptotic solution for ② is in fair agreement with numerical simulations for this case as well. We note that a small discrepancy exists even for the Newtonian case ($De = 0$), thus indicating that the error is due to the non-fulfillment of the lubrication assumptions rather than the low-*De* analysis.

Unlike ②, the ④ term strongly depends on *De*, and both our third-order asymptotic solution (red dashed lines) and numerical simulations (triangles) predict a monotonic decrease with *De*, which is the main source of reduction in the pressure drop observed in figure 2. We, therefore, may conclude that for narrow configurations, such as those shown in figure 1, the dimensionless pressure drop, calculated along $Y = 0$, is determined from the balance between the ② and ④ terms and the reduction in the pressure drop for contracting channels is due to the viscoelastic viscous shear stress term ④.

At this point, the reader might ask why we observe the pressure drop reduction for the Oldroyd-B fluid in contracting channels. To explain this, let us look at the expression for the pressure gradient along the channel. Using (3.6) and (3.15), the pressure gradient $\mathrm{d}P/\mathrm{d}Z$ is approximately

$$\frac{\mathrm{d}P}{\mathrm{d}Z} = -\frac{3}{H(Z)^3}\left(1 + \frac{6\tilde{\beta}De}{H(Z)^2}\frac{\mathrm{d}H(Z)}{\mathrm{d}Z}\right) + O(De^2, \epsilon^2), \tag{5.4}$$

which can be rewritten in a dimensional form as

$$\frac{\mathrm{d}p}{\mathrm{d}z} \approx -\frac{3q}{2h(z)^3}\underbrace{\eta_0\left(1 + \frac{\eta_p}{\eta_0}\frac{3\lambda q}{h(z)^2}\frac{\mathrm{d}h(z)}{\mathrm{d}z}\right)}_{\eta_{eff}}, \tag{5.5}$$

where we have introduced an 'effective viscosity' η_{eff}, by analogy with the constant viscosity η_0 appearing in the classical lubrication result in the case of a Newtonian fluid, i.e. $\mathrm{d}p/\mathrm{d}z = -(3/2)q\eta_0/h(z)^3$. For contracting channels ($\mathrm{d}h(z)/\mathrm{d}z < 0$), from (5.5) it follows that $\eta_{eff} < \eta_0$, and thus the pressure gradient and pressure drop for the Oldroyd-B fluid are less than for corresponding Newtonian case. Similarly, for expanding

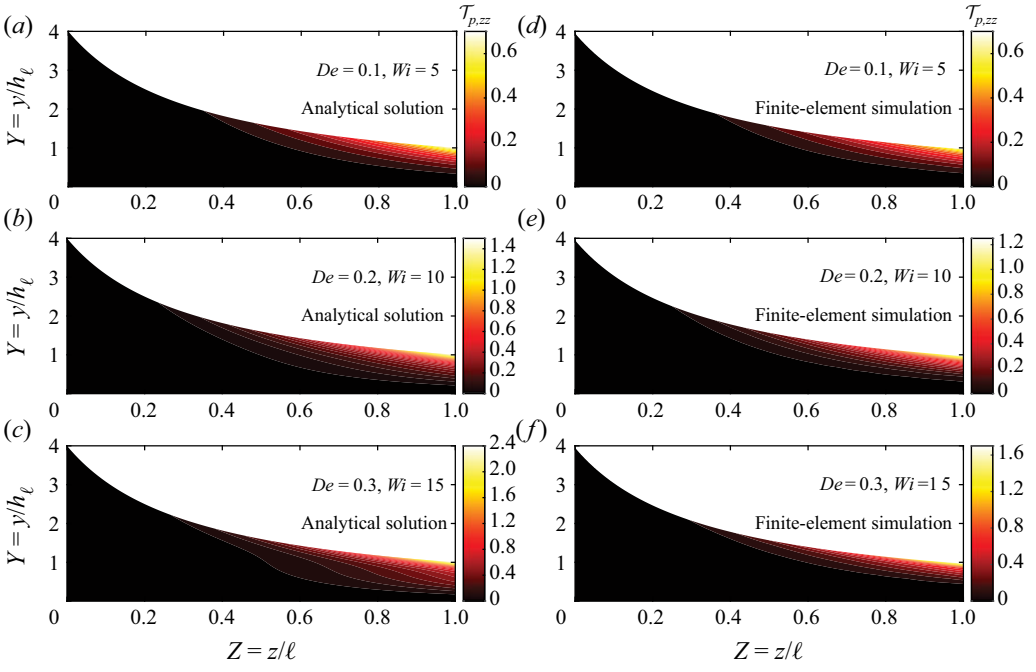

Figure 4. Contour plot of the axial polymer stress distribution, $\mathcal{T}_{p,zz}$, as a function of the (Y, Z) coordinates for (*a*,*d*) $De = 0.1$ ($Wi = 5$), (*b*,*e*) $De = 0.2$ ($Wi = 10$) and (*c*,*f*) $De = 0.3$ ($Wi = 15$), obtained from (*a–c*) our analytical theory and (*d–f*) 2-D numerical simulations. All calculations were performed using $\epsilon = 0.02$, $\alpha = 4$, and $\tilde{\beta} = 0.4$.

channels ($\mathrm{d}h(z)/\mathrm{d}z > 0$), η_{eff} is greater than η_0, and (5.5) predicts an increase in the pressure drop, in qualitative agreement with 2-D numerical simulations using the Oldroyd-B model for abruptly expanding channels (Binding *et al.* 2006). For a discussion on the Lagrangian-based micro-structure interpretation of the pressure drop reduction mechanism in contracting channels, we further refer the reader to work of Szabo *et al.* (1997) and a lecture of Hinch (2010).

5.3. *Comparison between the analytical predictions and the 2-D numerical simulations for the axial velocity and polymer stress contributions*

The theoretical results derived in § 3 allow closed-form analytical expressions to be determined for the velocity and pressure, as well as solvent and polymer stress distributions, which can then be compared with the results of numerical simulations. It is of particular interest to compare the results for the polymer stress distribution, especially the $\mathcal{T}_{p,zz}$ and $\mathcal{T}_{p,yz}$ components, whose gradients contribute to the axial pressure gradient, ultimately resulting in the pressure drop. Due to symmetry along the $Y = 0$, in the following we show the polymer stress and velocity distributions only in the half domain, $Y \geq 0$.

We present in figures 4 and 5 a comparison of our analytical predictions (*a–c*) and finite-element simulation results (*d–f*) for the axial and shear polymer stress distribution, $\mathcal{T}_{p,zz}$ and $\mathcal{T}_{p,yz}$, respectively, for different values of De, with $\epsilon = 0.02$, $\alpha = 4$, and $\tilde{\beta} = 0.4$. Clearly, for $De = 0.1$ and $De = 0.2$ there is good agreement between our analytical predictions and the numerical results for both $\mathcal{T}_{p,zz}$ and $\mathcal{T}_{p,yz}$. However, as expected,

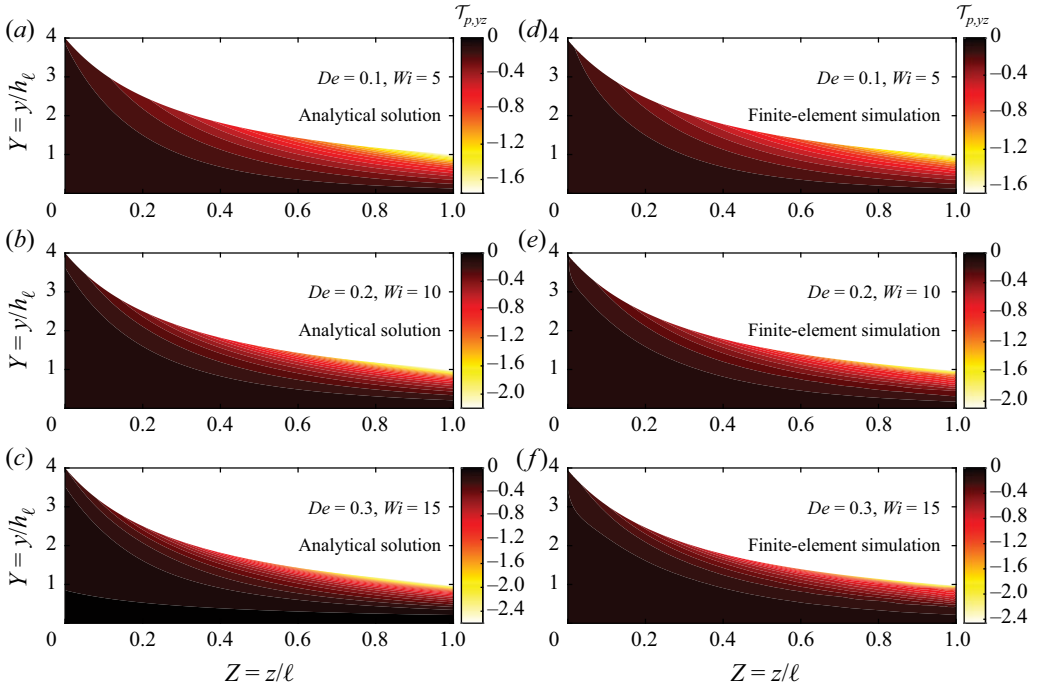

Figure 5. Contour plot of the polymer shear stress distribution, $\mathcal{T}_{p,yz}$, as a function of the (Y, Z) coordinates for (*a*,*d*) $De = 0.1$ ($Wi = 5$), (*b*,*e*) $De = 0.2$ ($Wi = 10$) and (*c*,*f*) $De = 0.3$ ($Wi = 15$), obtained from (*a–c*) our analytical theory and (*d–f*) 2-D numerical simulations. All calculations were performed using $\epsilon = 0.02$, $\alpha = 4$, and $\tilde{\beta} = 0.4$.

when De increases, the agreement deteriorates, and for $De = 0.3$, our analytical solution overpredicts the magnitude of $\mathcal{T}_{p,zz}$ and $\mathcal{T}_{p,yz}$ on the wall and does not capture exactly the polymer stress distribution in the entire domain. As $\mathcal{T}_{p,yz}$ and $\mathcal{S}_{yz}$ are related through (2.16*b*), the latter observation is consistent with the discrepancy between theory and simulations observed for $De = 0.3$ in figure 3(*a*) for the pressure drop contribution related to the $\partial \mathcal{S}_{yz}/\partial Y$ (term ④).

It is evident from figures 4 and 5 that $\mathcal{T}_{p,zz}$ is positive and $\mathcal{T}_{p,yz}$ is negative for $Y > 0$, with a minimum magnitude on the centreline and a maximum magnitude on the wall at the outlet, i.e. $(Y, Z) = (1, 1)$. These results and the $\mathcal{T}_{p,zz}$ and $\mathcal{T}_{p,yz}$ distributions are in qualitative agreement with the numerical results of Nyström *et al.* (2016) for the axial and shear polymer stress contributions of a viscoelastic fluid, described by the FENE-CR model, in an axisymmetric contracting hyperbolic channel, shown in their figures 7(*b*) and 7(*c*). It is also worth noting that all of the presented analytical and numerical results here for $\mathcal{T}_{p,zz}$ and $\mathcal{T}_{p,yz}$ are $O(1)$, thus clearly showing that our scalings in (2.10*c*) and (2.10*d*) for narrow geometries are representative, consistent with the studies on thin films and lubrication problems (Tichy 1996; Zhang *et al.* 2002; Saprykin *et al.* 2007; Ahmed & Biancofiore 2021). We note that in most studies all the components of the polymer stress tensor were scaled with the same scaling $\eta_0 u_c/h_\ell$. While such a scaling holds for geometries with $h_\ell/\ell = O(1)$, for narrow geometries it becomes inappropriate.

Although the viscoelastic axial stress is negligible along the centreline and, thus, has a minor contribution to the pressure drop calculated along $Y = 0$ (see figure 3), figure 4 clearly shows that $\mathcal{T}_{p,zz}$ is non-negligible in the rest of the domain. In fact, using the results

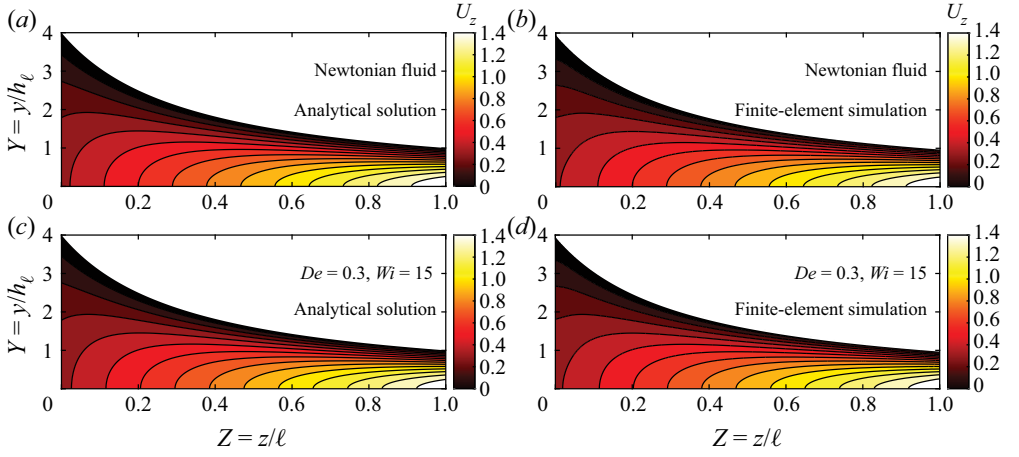

Figure 6. Comparison of (*a*,*c*) analytical predictions and (*b*,*d*) finite-element simulation results for contours of the axial velocity, U_z, as a function of the (Y, Z) coordinates for (*a*,*b*) the Newtonian fluid and (*c*,*d*) Oldroyd-B fluid with $De = 0.3$ ($Wi = 15$) in the case of a hyperbolic contracting channel. All calculations were performed using $\epsilon = 0.02$, $\alpha = 4$ and $\tilde{\beta} = 0.4$.

of §§ 2.1, 3.1 and 3.2, we obtain that the polymer stress tensor in the dimensional form, $\boldsymbol{\tau}_p$, in the weakly viscoelastic and lubrication limits is approximately

$$\boldsymbol{\tau}_p \approx \frac{\eta_p}{\lambda} \begin{pmatrix} Wi^2 \dfrac{18Y^2}{H(Z)^6} & -Wi \dfrac{3Y}{H(Z)^3} \\ -Wi \dfrac{3Y}{H(Z)^3} & 3\epsilon Wi \dfrac{\mathrm{d}H(Z)}{\mathrm{d}Z} \dfrac{(-3Y^2 + H(Z)^2)}{H(Z)^4} \end{pmatrix}, \tag{5.6}$$

where Wi is $O(1)$. Under the assumptions that Y, $H(Z)$, and $\mathrm{d}H(Z)/\mathrm{d}Z$ are $O(1)$, from (5.6) it follows that $\tau_{p,zz}$ can be comparable or larger than the shear stress $\tau_{p,yz}$. However, for narrow geometries, $\tau_{p,yy}$ is much smaller than $\tau_{p,zz}$ and $\tau_{p,yz}$ because it scales as $O(\epsilon)$.

In addition to the polymer stress distribution, we compare our analytical predictions for the axial velocity with the results of the numerical simulations. Figure 6 shows a comparison of analytical predictions (figures 6*a* and 6*c*) and finite-element simulation results (figures 6*b* and 6*d*) for contours of the axial velocity, U_z, as a function of the (Y, Z) coordinates for the Newtonian fluid (figures 6*a* and 6*b*) and Oldroyd-B fluid (figures 6*c* and 6*d*) with $De = 0.3$ ($Wi = 15$), $\epsilon = 0.02$, $\alpha = 4$ and $\tilde{\beta} = 0.4$. First, we observe excellent agreement between the analytical and numerical results for the axial velocity U_z for both $De = 0$ (Newtonian case) and $De = 0.3$. Second, and more importantly, the axial velocity distribution for $De = 0.3$ seems nearly identical to the Newtonian case, which might seem surprising given the observed pressure drop reduction for $De = 0.3$. As we noted in § 5.2, the reason for this behaviour is the weak dependence of the velocity on the Deborah number, so that the viscoelastic effects start to affect the flow field only at $O(De^2)$ and higher orders.

5.4. *Effect of the inlet-to-outlet aspect ratio and polymer-to-solvent viscosity ratio*

In this section, we explore the effect of the inlet-to-outlet aspect ratio $\alpha = h_0/h_\ell$ and polymer-to-solvent viscosity ratio η_p/η_s on the pressure drop. First, in figures 7(*a*) and 7(*b*)

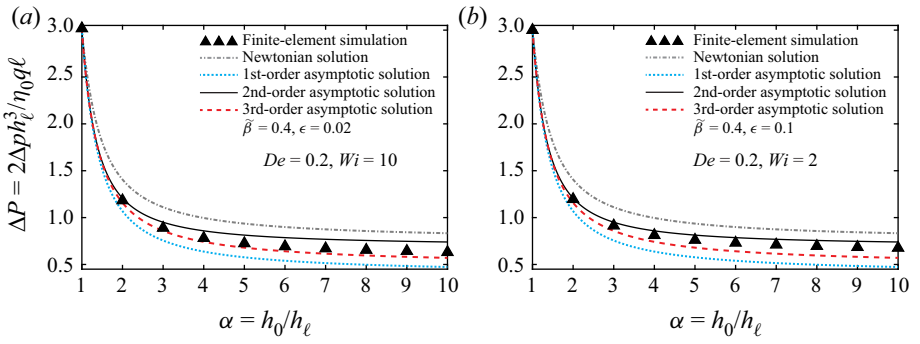

Figure 7. The effect of the inlet-to-outlet ratio $\alpha = h_0/h_\ell$ on the non-dimensional pressure drop of the Oldroyd-B fluid in a hyperbolic contracting channel. (*a*) Dimensionless pressure drop ΔP as a function of α for $\epsilon = 0.02$ and $De = 0.2$ ($Wi = 10$). (*b*) Dimensionless pressure drop ΔP as a function of α for $\epsilon = 0.1$ and $De = 0.2$ ($Wi = 2$). Black triangles (▲) represent the results of the finite-element simulations. Grey dash-dotted (- · -) lines represent the Newtonian solution, given by (5.2*a*). Cyan dotted (· · · ·) lines represent the first-order asymptotic solution, given by (5.2*a*)–(5.2*b*). Black solid (—) lines represent the second-order asymptotic solution, given by (5.2*a*)–(5.2*c*). Red dashed (- -) lines represent the third-order asymptotic solution, given by (5.2*a*)–(5.2*d*). All calculations were performed using $\tilde{\beta} = 0.4$.

we present the non-dimensional pressure drop $\Delta P = \Delta p/(\eta_0 q\ell/2h_\ell^3)$ as a function of α for $\epsilon = 0.02$ (*a*) and $\epsilon = 0.1$ (*b*), with $De = 0.2$ and $\tilde{\beta} = 0.4$. Grey dash-dotted lines represent the leading-order (Newtonian) asymptotic solution, given by (5.2*a*), and as earlier, cyan dotted lines represent the first-order asymptotic solution, given by (5.2*a*)–(5.2*b*), black solid lines represent the second-order asymptotic solution, given by (5.2*a*)–(5.2*c*), and red dashed lines represent the third-order asymptotic solution, given by (5.2*a*)–(5.2*d*). Black triangles represent the results of the numerical simulations. As expected, when increasing $\alpha = h_0/h_\ell$ (or h_0), while fixing the values of h_ℓ and q, the $\Delta P = \Delta p/(\eta_0 q\ell/2h_\ell^3)$, which can be viewed as the dimensionless hydrodynamic resistance, monotonically decreases. Moreover, for a given value of $\alpha = h_0/h_\ell$, the pressure drop of the Oldroyd-B fluid is smaller than that of a Newtonian fluid, consistent with the results of figure 2.

For small values of α, figure 7(*a*,*b*) shows good agreement between the third-order asymptotic solution and numerical simulation results for both $\epsilon = 0.02$ and $\epsilon = 0.1$. However, as α increases, the agreement between the theory and simulations deteriorates because the assumptions of the lubrication theory become less well satisfied. Nevertheless, even the case of $\alpha = 10$ results in relative errors of only approximately 10 % and 16 % for $\epsilon = 0.02$ and $\epsilon = 0.1$, respectively. The latter result for $\epsilon = h_\ell/\ell = 0.1$ and $\alpha\epsilon = h_0/\ell = 1$ clearly indicates that our theory is applicable not only to narrow geometries but also can be used for geometries with a high aspect ratio, and can still reasonably predict the dimensionless pressure drop.

Finally, we consider the effect of the polymer-to-solvent viscosity ratio η_p/η_s on the pressure drop in figures 8(*a*) and 8(*b*) for $\epsilon = 0.02$ and $\epsilon = 0.1$, respectively, with $De = 0.1$ and $\alpha = 4$. We note that it is of more practical interest to discuss the effect of η_p/η_s rather than $\tilde{\beta} = \eta_p/\eta_0$, because typically in the experiments the viscosity of the solvent η_s remains fixed, while the polymer viscosity η_p may change through modifying the polymer concentration, and thus the total viscosity $\eta_0 = \eta_s + \eta_p$ may also vary. Now, as η_0 varies, we find it is more appropriate to present in figures 8(*a*) and 8(*b*) the pressure drop Δp scaled by $\eta_s q\ell/2h_\ell^3$, which is $\Delta P/(1-\tilde{\beta})$, rather than ΔP. It is evident from figures 8(*a*) and 8(*b*) that for a given value of De (or Wi), the pressure drop increases linearly with

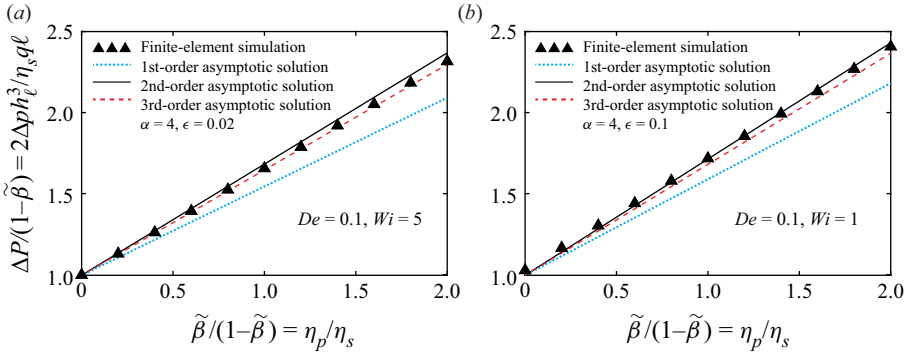

Figure 8. The effect of the polymer contribution to the viscosity on the pressure drop of the Oldroyd-B fluid in a hyperbolic contracting channel. (*a*) Pressure drop Δp scaled by $\eta_s q\ell/2h_\ell^3$ as a function of the polymer to solvent viscosity ratio η_p/η_s for $\epsilon = 0.02$ and $De = 0.1$ ($Wi = 5$). (*b*) Pressure drop Δp scaled by $\eta_s q\ell/2h_\ell^3$ as a function of the polymer to solvent viscosity ratio η_p/η_s for $\epsilon = 0.1$ and $De = 0.1$ ($Wi = 1$). Black triangles (▲) represent the results of the finite-element simulation. Cyan dotted (· · ·) lines represent the first-order asymptotic solution, given by (5.2*a*)–(5.2*b*). Black solid (—) lines represent the second-order asymptotic solution, given by (5.2*a*)–(5.2*c*). Red dashed (- -) lines represent the third-order asymptotic solution, given by (5.2*a*)–(5.2*d*). All calculations were performed using $\alpha = 4$.

η_p/η_s. This behaviour can be explained using (5.3) and noting that the first and third terms have negligible contribution to the pressure drop, as shown in figure 3, so that $\Delta P/(1-\tilde{\beta})$ is approximately

$$\frac{\Delta P}{1-\tilde{\beta}} \approx \underbrace{\left(1+\frac{\eta_p}{\eta_s}\right)\int_1^0 \left.\frac{\partial^2 U_z}{\partial Y^2}\right|_{Y=0} \mathrm{d}Z}_{②} + \underbrace{\frac{\eta_p}{\eta_s} De \int_1^0 \left.\frac{\partial \mathcal{S}_{yz}}{\partial Y}\right|_{Y=0} \mathrm{d}Z}_{④}, \tag{5.7}$$

clearly showing that $\Delta P/(1-\tilde{\beta})$ scales linearly with η_p/η_s.

For $\epsilon = 0.02$, we observe a good agreement between the third-order asymptotic solution (red dashed line) and numerical simulation results (black triangles). For $\epsilon = 0.1$, however, the third-order asymptotic solution slightly underpredicts the numerically obtained pressure drop, consistent with our previous results shown in figure 2(*b*). Nevertheless, the resulting relative error is below 5 % throughout the investigated range of parameters.

6. Concluding remarks

In this work, we have studied the pressure-driven flow of an Oldroyd-B fluid in arbitrarily shaped, narrow channels and developed a theoretical framework for calculating the velocity and stress fields and the q–Δp relation. Using the lubrication approximation, we first identified the appropriate characteristic scales and dimensionless parameters governing the viscoelastic flow in narrow geometries. We then employed a perturbation expansion in powers of De and provided analytical expressions for the velocity and stress fields and the flow rate–pressure drop relation in the weakly viscoelastic limit up to $O(De^2)$. We further exploited the reciprocal theorem to obtain the q–Δp relation at the next order, $O(De^3)$, using only the velocity and stress fields at the previous orders, eliminating the need to solve the viscoelastic flow problem at $O(De^3)$.

To validate the results of our theoretical model, we performed 2-D numerical simulations of the viscoelastic flow, described by the Oldroyd-B model, in a hyperbolic,

symmetric contracting channel for the flow-rate-controlled situation. For geometries that satisfy well the lubrication assumptions, we found excellent agreement between the velocity, polymer stress and pressure drop predicted by our theory and those obtained from the numerical simulations. Furthermore, we showed that our theory is applicable not only to narrow geometries but it also can be used for geometries with a high aspect ratio, while still reasonably predicting the pressure drop in the weakly viscoelastic limit.

Both our theory and simulations showed a weak dependence of the velocity field of an Oldroyd-B fluid on the Deborah number so that it can be approximated as Newtonian. In contrast, we have demonstrated that the dimensionless pressure drop of an Oldroyd-B fluid strongly depends on the viscoelastic effects and monotonically decreases with increasing De, similar to previous numerical reports on 2-D abruptly contracting geometries (Aboubacar *et al.* 2002; Alves *et al.* 2003; Binding *et al.* 2006; Aguayo *et al.* 2008). To understand the cause for such pressure drop reduction, which has been largely unexplored to date, we elucidated the relative importance of different terms contributing to the pressure drop along the symmetry line (see (5.3)). We identified that a pressure drop reduction for narrow contracting geometries is primarily due to viscoelastic shear stresses gradients (term ④ in (5.3)), while viscoelastic axial stresses (term ③ in (5.3)) make a negligible contribution to the pressure drop, calculated along the symmetry line. However, although for narrow geometries the viscoelastic axial stresses are negligible along the symmetry line, they are comparable or larger than shear stresses in the rest of the domain, as shown in § 5.3.

In this work, we have used the lubrication theory to calculate analytically the flow rate–pressure drop relation of Oldroyd-B fluids in narrow geometries in the weakly viscoelastic limit. We showed that our approach holds well even for channels with the contraction amplitude comparable to or larger than the channel height (see figure 7). Understanding the behaviour at a higher Deborah number requires numerically solving the lubrication equations on a non-rectangular domain, which may involve cumbersome implementation using finite differences. We note that beyond lubrication theory, other approaches, such as the domain decomposition method, have been exploited to study numerically the flow rate–pressure drop relation of the UCM and Oldroyd-B fluids in undulating channels (Pilitsis & Beris 1989; Souvaliotis & Beris 1992). The domain decomposition method is convenient for numerical implementation since it maps and solves the problem with 'complex' geometry on a rectangular domain (Tang, Haynes & Houzeaux 2020). However, this method is limited to geometries in which the amplitude of contraction/undulation is much smaller than the channel height (Pilitsis & Beris 1989; Souvaliotis & Beris 1992).

Our theoretical approach is not restricted to the case of 2-D channels and can be utilised to calculate the flow rate–pressure drop relation in narrow axisymmetric geometries. We also expect our results to directly apply to narrow and shallow 3-D channels of length ℓ, width w and height h, where $h \ll w \ll \ell$, or $h/\ell \ll 1$ and $h/w \ll 1$. Nevertheless, further investigation would be required to assess the range of validity of this approximation.

One interesting extension of the present work, which relies on the leading-order lubrication theory, is to calculate the high-order perturbative corrections to the pressure drop, following, e.g., Tavakol *et al.* (2017). We anticipate that with such corrections, our framework will allow accurate prediction of the pressure drop in geometries with a modest aspect ratio and rapidly varying shape. Finally, while we considered the Oldroyd-B model to describe the viscoelasticity and predicted a monotonic reduction in the pressure drop with increasing De for contracting geometries, as a future research direction, it is interesting to analyse more complex constitutive models that incorporate additional microscopic features of polymer solutions and to study the effect of these features on

the pressure drop. Although a more complex model may pose significant challenges for analytical progress, we anticipate the theoretical framework presented here may still allow the development of a simplified, reduced-order model, amenable to asymptotic/numerical investigations.

Acknowledgements. We thank C.A. Browne, S.S. Datta, E.J. Hinch and L.G. Leal for helpful discussions. We thank D. Ilssar and D.M. Kochmann for providing us with the computational facilities for performing numerical simulations.

Funding. This research was partially supported by NSF through the Princeton University's Materials Research Science and Engineering Center DMR-2011750. E.B. acknowledges the support of the Yad Hanadiv (Rothschild) Foundation and the Zuckerman STEM Leadership Program.

Declaration of interests. The authors report no conflict of interest.

Author ORCIDs.
Evgeniy Boyko https://orcid.org/0000-0002-9202-5154;
Howard A. Stone https://orcid.org/0000-0002-9670-0639.

Appendix A. Details of numerical simulations

In this appendix we describe the numerical techniques used to solve the system of (2.1), (2.2) and (2.5). We have performed 2-D finite-element numerical simulations using the viscoelastic flow module in COMSOL Multiphysics, which includes the Oldroyd-B constitutive model (version 5.6, COMSOL AB, Stockholm, Sweden). All the equations are written in weak form by means of the corresponding integral scalar product, defined in terms of test functions for the pressure, velocity and polymer stress fields, i.e. $\tilde{p}$, $\tilde{u}$ and $\tilde{\tau}_p$, respectively. Additional details of the finite-element formulation and weak form implementation for the Oldroyd-B model in COMSOL Multiphysics are given in Craven, Rees & Zimmerman (2006) and Rajagopal & Das (2016).

The symmetry of the channel allows us to simplify the problem to consider only half of the domain, as shown in figure 9. We impose the no-slip and the no-penetration boundary conditions along the wall, $y = h(z)$, and symmetry boundary condition along the centreline, $y = 0$. As we are interested in determining the pressure drop Δp originating from the contraction geometry, we have added two straight regions of length ℓ to eliminate the entrance and exit effects. Thus, we impose fully developed unidirectional Poiseuille velocity profile at the entrance and exit. In addition, at the entrance, we impose the polymer stress distribution corresponding to the Poiseuille flow. At the exit, the reference value for the pressure is set to zero on $y = 0$. Finally, we calculate the pressure drop along the centreline between the inlet ($z = 0$) and outlet ($z = \ell$) of the contraction, i.e. $\Delta p = p(y = 0, z = 0) - p(y = 0, z = \ell)$.

We summarise in table 2 the values of physical and geometrical parameters used in the numerical simulations. We mainly consider two hyperbolic geometries, which have an identical inlet-to-outlet ratio $\alpha = h_0/h_\ell = 4$ but different aspect ratios $\epsilon = h_\ell/\ell$: $\epsilon = 0.02$ (case I) and $\epsilon = 0.1$ (case II). In both cases, we keep $\ell = 5$ mm and $u_c = 5$ mm s^{-1}, while setting $h_\ell = 0.1$ mm (case I) and $h_\ell = 0.5$ mm (case II), and adjusting the flow rate per unit depth $q = 2h_\ell u_c$, accordingly. For each case, to the study the effect of different Deborah numbers, we change the relaxation time λ from 0 to 0.3 s to change De from 0 to 0.3, while keeping all other physical and geometrical parameters. When investigating the effect of the inlet-to-outlet ratio $\alpha = h_0/h_\ell$ on the pressure drop, we change only the value of h_0 for each of the cases I and II and set $\lambda = 0.2$ s, corresponding to $De = 0.2$, while keeping the values of all other parameters. Similarly, when studying the effect of the polymer-to-solvent viscosity ratio η_p/η_s on the pressure drop, we change only the value

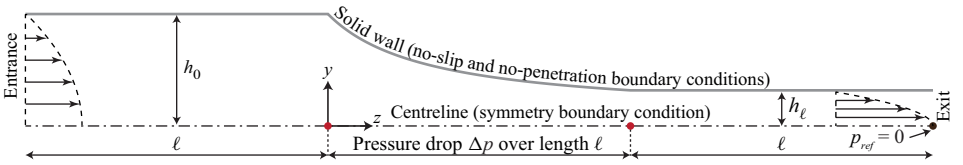

Figure 9. Schematic illustration of the 2-D hyperbolic contracting channel with straight entrance and exit regions of length ℓ used in finite-element numerical simulations for the pressure-driven flow of the Oldroyd-B fluid.

ℓ (mm)	η_0 (Pa s)	η_s (Pa s)	η_p (Pa s)	u_c (mm s^{-1})	ρ (kg m^{-3})	λ (s)	De	$\tilde{\beta}$	α
5	1	0.6	0.4	5	1	0 – 0.3	0–0.3	0.4	4
	ϵ	h_0 (mm)	h_ℓ (mm)	q (m^2 s^{-1})	p_c (Pa)	Wi	Re		
Case I	0.02	0.4	0.1	10^{-6}	2500	0–15	5×10^{-7}		
Case II	0.1	2	0.5	5×10^{-6}	100	0–3	2.5×10^{-6}		

Table 2. Values of physical parameters used in the 2-D numerical simulations of the pressure-driven flow of the Oldroyd-B fluid in a hyperbolic contracting channel. The Reynolds number Re is defined as $Re = \rho u_c h_\ell/\eta_0$ and the characteristic pressure p_c is given as $p_c = \eta_0 u_c \ell/h_\ell^2$.

of η_p for each of the cases I and II, while setting $\eta_s = 1$ Pa s and $\lambda = 0.1$ s ($De = 0.1$), and keeping the values of all other parameters. We note that while the steady momentum equations in COMSOL Multiphysics have a convective term, the effect of fluid inertia is negligible in our simulations, as the Reynolds number is vanishingly small; see table 2.

We discretised the velocity field using the second-order Lagrange elements and the pressure and polymer stress fields using the first-order Lagrange elements, resulting in meshes of $\approx 84\,000$ elements for $\epsilon = 0.02$ and $\approx 17\,000$ elements for $\epsilon = 0.1$. We performed tests to assess the grid sensitivity at this resolution and established grid independence. Finally, the PARDISO solver implemented in COMSOL Multiphysics has been used for simulation and the relative tolerance of the nonlinear method is always set to 10^{-5}.

References

Aboubacar, M., Matallah, H. & Webster, M.F. 2002 Highly elastic solutions for Oldroyd-B and Phan-Thien/Tanner fluids with a finite volume/element method: planar contraction flows. *J. Non-Newtonian Fluid Mech.* **103** (1), 65–103.

Afonso, A.M., Oliveira, P.J., Pinho, F.T. & Alves, M.A. 2011 Dynamics of high-Deborah-number entry flows: a numerical study. *J. Fluid Mech.* **677**, 272–304.

Aguayo, J.P., Tamaddon-Jahromi, H.R. & Webster, M.F. 2008 Excess pressure-drop estimation in contraction and expansion flows for constant shear-viscosity, extension strain-hardening fluids. *J. Non-Newtonian Fluid Mech.* **153** (2-3), 157–176.

Ahmed, H. & Biancofiore, L. 2021 A new approach for modeling viscoelastic thin film lubrication. *J. Non-Newtonian Fluid Mech.* **292**, 104524.

Allmendinger, A., Fischer, S., Huwyler, J., Mahler, H.C., Schwarb, E., Zarraga, I.E. & Mueller, R. 2014 Rheological characterization and injection forces of concentrated protein formulations: an alternative predictive model for non-Newtonian solutions. *Eur. J. Pharm. Biopharm.* **87** (2), 318–328.

Alves, M.A., Oliveira, P.J. & Pinho, F.T. 2003 Benchmark solutions for the flow of Oldroyd-B and PTT fluids in planar contractions. *J. Non-Newtonian Fluid Mech.* **110** (1), 45–75.

ALVES, M.A., OLIVEIRA, P.J. & PINHO, F.T. 2021 Numerical methods for viscoelastic fluid flows. *Annu. Rev. Fluid Mech.* **53**, 509–541.

ALVES, M.A. & POOLE, R.J. 2007 Divergent flow in contractions. *J. Non-Newtonian Fluid Mech.* **144** (2–3), 140–148.

BINDING, D.M., PHILLIPS, P.M. & PHILLIPS, T.N. 2006 Contraction/expansion flows: the pressure drop and related issues. *J. Non-Newtonian Fluid Mech.* **137** (1–3), 31–38.

BIRD, R.B., ARMSTRONG, R.C. & HASSAGER, O. 1987 *Dynamics of Polymeric Liquids, Volume 1: Fluid Mechanics*, 2nd edn. John Wiley and Sons.

BLACK, J.R. & DENN, M.M. 1976 Converging flow of a viscoelastic liquid. *J. Non-Newtonian Fluid Mech.* **1** (1), 83–92.

BOYKO, E. & STONE, H.A. 2021 Reciprocal theorem for calculating the flow rate–pressure drop relation for complex fluids in narrow geometries. *Phys. Rev. Fluids* **6**, L081301.

CAMPO-DEAÑO, L., GALINDO-ROSALES, F.J., PINHO, F.T., ALVES, M.A. & OLIVEIRA, M.S.N. 2011 Flow of low viscosity Boger fluids through a microfluidic hyperbolic contraction. *J. Non-Newtonian Fluid Mech.* **166** (21-22), 1286–1296.

CHILCOTT, M.D. & RALLISON, J.M. 1988 Creeping flow of dilute polymer solutions past cylinders and spheres. *J. Non-Newtonian Fluid Mech.* **29**, 381–432.

CRAVEN, T.J., REES, J.M. & ZIMMERMAN, W.B. 2006 Stabilised finite element modelling of Oldroyd-B viscoelastic flows. In *COMSOL Conference*. Birmingham.

DATTA, S.S., *et al.* 2021 Perspectives on viscoelastic flow instabilities and elastic turbulence (preprint) arXiv:2108.09841.

DEBBAUT, B., MARCHAL, J.M. & CROCHET, M.J. 1988 Numerical simulation of highly viscoelastic flows through an abrupt contraction. *J. Non-Newtonian Fluid Mech.* **29**, 119–146.

FISCHER, I., SCHMIDT, A., BRYANT, A. & BESHEER, A. 2015 Calculation of injection forces for highly concentrated protein solutions. *Intl J. Pharm.* **493** (1-2), 70–74.

GIESEKUS, H. 1963 Die simultane translations-und rotationsbewegung einer Kugel in einer elastoviskosen Flüssigkeit. *Rheol. Acta* **3** (1), 59–71.

GROISMAN, A. & QUAKE, S.R. 2004 A microfluidic rectifier: anisotropic flow resistance at low Reynolds numbers. *Phys. Rev. Lett.* **92** (9), 094501.

GROISMAN, A. & STEINBERG, V. 1996 Couette-Taylor flow in a dilute polymer solution. *Phys. Rev. Lett.* **77** (8), 1480.

HINCH, E.J. 2010 Otto Laporte lecture: explaining the flow of elastic liquid. In *63rd Annual Meeting of the APS Division of Fluid Dynamics*. American Physical Society.

HSIAO, K.W., DINIC, J., REN, Y., SHARMA, V. & SCHROEDER, C.M. 2017 Passive non-linear microrheology for determining extensional viscosity. *Phys. Fluids* **29** (12), 121603.

JAMES, D.F. 2016 N1 stresses in extensional flows. *J. Non-Newtonian Fluid Mech.* **232**, 33–42.

JAMES, D.F. & ROOS, C.A.M. 2021 Pressure drop of a boger fluid in a converging channel. *J. Non-Newtonian Fluid Mech.* **293**, 104557.

KEILLER, R.A. 1993 Entry-flow calculations for the Oldroyd-B and FENE equations. *J. Non-Newtonian Fluid Mech.* **46** (2–3), 143–178.

KESHAVARZ, B. & MCKINLEY, G.H. 2016 Micro-scale extensional rheometry using hyperbolic converging/diverging channels and jet breakup. *Biomicrofluidics* **10** (4), 043502.

KEUNINGS, R. 2004 Micro-macro methods for the multiscale simulation of viscoelastic flow using molecular models of kinetic theory. *Rheol. Rev.* **2004**, 67–98.

KOPPOL, A.P., SURESHKUMAR, R., ABEDIJABERI, A. & KHOMAMI, B. 2009 Anomalous pressure drop behaviour of mixed kinematics flows of viscoelastic polymer solutions: a multiscale simulation approach. *J. Fluid Mech.* **631**, 231–253.

LARSON, R.G. 1992 Instabilities in viscoelastic flows. *Rheol. Acta* **31** (3), 213–263.

LÓPEZ-AGUILAR, J.E., TAMADDON-JAHROMI, H.R., WEBSTER, M.F. & WALTERS, K. 2016 Numerical vs experimental pressure drops for Boger fluids in sharp-corner contraction flow. *Phys. Fluids* **28** (10), 103104.

MOROZOV, A. & SPAGNOLIE, S.E. 2015 Introduction to complex fluids. In *Complex Fluids in Biological Systems* (ed. S.E. Spagnolie), pp. 3–52. Springer.

NGUYEN, N.T., LAM, Y.C., HO, S.S. & LOW, C.L.N. 2008 Improvement of rectification effects in diffuser/nozzle structures with viscoelastic fluids. *Biomicrofluidics* **2** (3), 034101.

NIGEN, S. & WALTERS, K. 2002 Viscoelastic contraction flows: comparison of axisymmetric and planar configurations. *J. Non-Newtonian Fluid Mech.* **102** (2), 343–359.

NYSTRÖM, M., TAMADDON-JAHROMI, H.R., STADING, M. & WEBSTER, M.F. 2012 Numerical simulations of Boger fluids through different contraction configurations for the development of a measuring system for extensional viscosity. *Rheol. Acta* **51** (8), 713–727.

NYSTRÖM, M., TAMADDON-JAHROMI, H.R., STADING, M. & WEBSTER, M.F. 2016 Extracting extensional properties through excess pressure drop estimation in axisymmetric contraction and expansion flows for constant shear viscosity, extension strain-hardening fluids. *Rheol. Acta* **55** (5), 373–396.

NYSTRÖM, M., TAMADDON-JAHROMI, H.R., STADING, M. & WEBSTER, M.F. 2017 Hyperbolic contraction measuring systems for extensional flow. *Mech. Time-Dependent Mater.* **21** (3), 455–479.

OBER, T.J., HAWARD, S.J., PIPE, C.J., SOULAGES, J. & MCKINLEY, G.H. 2013 Microfluidic extensional rheometry using a hyperbolic contraction geometry. *Rheol. Acta* **52** (6), 529–546.

OLIVEIRA, M.S.N., OLIVEIRA, P.J., PINHO, F.T. & ALVES, M.A. 2007 Effect of contraction ratio upon viscoelastic flow in contractions: the axisymmetric case. *J. Non-Newtonian Fluid Mech.* **147** (1-2), 92–108.

OWENS, R.G. & PHILLIPS, T.N. 2002 *Computational Rheology*. Imperial College Press.

PEARSON, J.R.A. 1985 *Mechanics of Polymer Processing*. Elsevier.

PÉREZ-SALAS, K.Y., SÁNCHEZ, S., ASCANIO, G. & AGUAYO, J.P. 2019 Analytical approximation to the flow of a sPTT fluid through a planar hyperbolic contraction. *J. Non-Newtonian Fluid Mech.* **272**, 104160.

PHAN-THIEN, N. 1978 A nonlinear network viscoelastic model. *J. Rheol.* **22** (3), 259–283.

PHAN-THIEN, N. & TANNER, R.I. 1977 A new constitutive equation derived from network theory. *J. Non-Newtonian Fluid Mech.* **2** (4), 353–365.

PILITSIS, S. & BERIS, A.N. 1989 Calculations of steady-state viscoelastic flow in an undulating tube. *J. Non-Newtonian Fluid Mech.* **31** (3), 231–287.

RAJAGOPAL, M.C. & DAS, S.K. 2016 Analyses of drag on viscoelastic liquid infused bio-inspired patterned surfaces. *J. Non-Newtonian Fluid Mech.* **228**, 17–30.

RALLISON, J.M. & KEILLER, R.A. 1993 Sink flows of a suspension of rigid rods: part 2. Lubrication theory. *J. Non-Newtonian Fluid Mech.* **48** (3), 237–259.

ROTHSTEIN, J.P. & MCKINLEY, G.H. 1999 Extensional flow of a polystyrene Boger fluid through a 4: 1: 4 axisymmetric contraction/expansion. *J. Non-Newtonian Fluid Mech.* **86** (1-2), 61–88.

ROTHSTEIN, J.P. & MCKINLEY, G.H. 2001 The axisymmetric contraction–expansion: the role of extensional rheology on vortex growth dynamics and the enhanced pressure drop. *J. Non-Newtonian Fluid Mech.* **98** (1), 33–63.

SAPRYKIN, S., KOOPMANS, R.J. & KALLIADASIS, S. 2007 Free-surface thin-film flows over topography: influence of inertia and viscoelasticity. *J. Fluid Mech.* **578**, 271–293.

SHAQFEH, E.S.G. 1996 Purely elastic instabilities in viscometric flows. *Annu. Rev. Fluid Mech.* **28** (1), 129–185.

SOUSA, P.C., COELHO, P.M., OLIVEIRA, M.S.N. & ALVES, M.A. 2009 Three-dimensional flow of Newtonian and Boger fluids in square–square contractions. *J. Non-Newtonian Fluid Mech.* **160** (2-3), 122–139.

SOUSA, P.C., PINHO, F.T., OLIVEIRA, M.S.N. & ALVES, M.A. 2010 Efficient microfluidic rectifiers for viscoelastic fluid flow. *J. Non-Newtonian Fluid Mech.* **165** (11-12), 652–671.

SOUVALIOTIS, A. & BERIS, A.N. 1992 Applications of domain decomposition spectral collocation methods in viscoelastic flows through model porous media. *J. Rheol.* **36** (7), 1417–1453.

STEINBERG, V. 2021 Elastic turbulence: an experimental view on inertialess random flow. *Annu. Rev. Fluid Mech.* **53**, 27–58.

SYKES, P. & RALLISON, J.M. 1997 Lubrication theory for a fibre suspension: part 1: pressure-driven flow in a planar channel having slowly-varying cross-section. *J. Non-Newtonian Fluid Mech.* **71** (1-2), 109–136.

SZABO, P., RALLISON, J.M. & HINCH, E.J. 1997 Start-up of flow of a FENE-fluid through a 4:1:4 constriction in a tube. *J. Non-Newtonian Fluid Mech.* **72** (1), 73–86.

TADMOR, Z. & GOGOS, C.G. 2013 *Principles of Polymer Processing*. John Wiley and Sons.

TAMADDON-JAHROMI, H.R., GARDUÑO, I.E., LÓPEZ-AGUILAR, J.E. & WEBSTER, M.F. 2016 Predicting large experimental excess pressure drops for Boger fluids in contraction–expansion flow. *J. Non-Newtonian Fluid Mech.* **230**, 43–67.

TAMADDON-JAHROMI, H.R., LÓPEZ-AGUILAR, J.E. & WEBSTER, M.F. 2018 On modelling viscoelastic flow through abrupt circular 8:1 contractions–matching experimental pressure-drops and vortex structures. *J. Non-Newtonian Fluid Mech.* **251**, 28–42.

TAMADDON-JAHROMI, H.R., WEBSTER, M.F. & WALTERS, K. 2010 Predicting numerically the large increases in extra pressure drop when Boger fluids flow through axisymmetric contractions. *J. Nat. Sci.* **2** (1), 1–11.

TAMADDON-JAHROMI, H.R., WEBSTER, M.F. & WILLIAMS, P.R. 2011 Excess pressure drop and drag calculations for strain-hardening fluids with mild shear-thinning: contraction and falling sphere problems. *J. Non-Newtonian Fluid Mech.* **166** (16), 939–950.

TANG, H.S., HAYNES, R.D. & HOUZEAUX, G. 2020 A review of domain decomposition methods for simulation of fluid flows: concepts, algorithms, and applications. *Arch. Comput. Meth. Engng* **28** (3), 841–873.

TANNER, R.I. 1966 Plane creeping flows of incompressible second-order fluids. *Phys. Fluids* **9** (6), 1246–1247.

TANNER, R.I. & PIPKIN, A.C. 1969 Intrinsic errors in pressure-hole measurements. *Trans. Soc. Rheol.* **13** (4), 471–484.

TAVAKOL, B., FROEHLICHER, G., HOLMES, D.P. & STONE, H.A. 2017 Extended lubrication theory: improved estimates of flow in channels with variable geometry. *Proc. R. Soc.* A **473** (2206), 20170234.

TICHY, J.A. 1996 Non-Newtonian lubrication with the convected Maxwell model. *Trans. ASME J. Tribol.* **118**, 344–348.

VARCHANIS, S., TSAMOPOULOS, J., SHEN, A.Q. & HAWARD, S.J. 2022 Reduced and increased flow resistance in shear-dominated flows of Oldroyd-B fluids. *J. Non-Newtonian Fluid Mech.* **300**, 104698.

WEBSTER, M.F., TAMADDON-JAHROMI, H.R., LÓPEZ-AGUILAR, J.E. & BINDING, D.M. 2019 Enhanced pressure drop, planar contraction flows and continuous spectrum models. *J. Non-Newtonian Fluid Mech.* **273**, 104184.

WHITE, J.L. & METZNER, A.B. 1963 Development of constitutive equations for polymeric melts and solutions. *J. Appl. Polym. Sci.* **7** (5), 1867–1889.

ZARGARTALEBI, A., ZARGARTALEBI, M. & BENNEKER, A.M. 2021 Analysis of vortices in viscoelastic fluid flow through confined geometries at low Reynolds numbers. *AIP Adv.* **11** (8), 085213.

ZHANG, Y.L., MATAR, O.K. & CRASTER, R.V. 2002 Surfactant spreading on a thin weakly viscoelastic film. *J. Non-Newtonian Fluid Mech.* **105** (1), 53–78.

ZOGRAFOS, K., HARTT, W., HAMERSKY, M., OLIVEIRA, M.S.N., ALVES, M.A. & POOLE, R.J. 2020 Viscoelastic fluid flow simulations in the e-VROC^{TM} geometry. *J. Non-Newtonian Fluid Mech.* **278**, 104222.